1 **A tissue-engineered human trabecular meshwork hydrogel for advanced glaucoma disease**
2 **modeling**

3

4 Haiyan Li[1,2,3], Tyler Bagué[1], Alexander Kirschner[1], Robert W. Weisenthal[1], Alison E.
5 Patteson[3,4], Nasim Annabi[5], W. Daniel Stamer[6], Preethi S. Ganapathy[1,3,7], Samuel
6 Herberg[1,2,3,8,9,*]

7

8 **Affiliations:**
9 [1]Department of Ophthalmology and Visual Sciences, SUNY Upstate Medical University,
10 Syracuse, NY 13210, USA
11 [2]Department of Cell and Developmental Biology, SUNY Upstate Medical University, Syracuse,
12 NY 13210, USA
13 [3]BioInspired Institute, Syracuse University, Syracuse, NY 13244, USA
14 [4]Department of Physics, Syracuse University, Syracuse, NY 13244, USA
15 [5]Department of Chemical and Biomolecular Engineering, University of California Los Angeles,
16 Los Angeles, CA 90095, USA
17 [6]Duke Eye Center, Duke University, Durham, NC 27708, USA
18 [7]Department of Neuroscience and Physiology, SUNY Upstate Medical University, Syracuse, NY
19 13210, USA
20 [8]Department of Biochemistry and Molecular Biology, SUNY Upstate Medical University,
21 Syracuse, NY 13210, USA
22 [9]Department of Biomedical and Chemical Engineering, Syracuse University, Syracuse, NY
23 13244, USA

24

25 *To whom correspondence should be addressed: Samuel Herberg, PhD, Assistant Professor;
26 Department of Ophthalmology and Visual Sciences, SUNY Upstate Medical University, 505
27 Irving Avenue, Neuroscience Research Building Room 4609, Syracuse, NY 13210, USA, email:
28 herbergs@upstate.edu

29

36

37 **Commercial relationships disclosures:** None.

38

39 **Keywords:** *In vitro*, bioengineering, tissue stiffening, ECM mechanics, POAG

40   **Abstract**

41   **Purpose:** Abnormal human trabecular meshwork (HTM) cell function and extracellular matrix

42   (ECM) remodeling contribute to HTM stiffening in primary open-angle glaucoma (POAG). Most

43   current cellular HTM model systems do not sufficiently replicate the complex native three

44   dimensional (3D) cell-ECM interface, which makes them less than ideal to investigate POAG

45   pathology. Tissue-engineered protein-based hydrogels are ideally positioned to overcome

46   shortcomings of current models. Here, we report a novel biomimetic HTM hydrogel and test its

47   utility as a POAG disease model.

48   **Methods:** HTM hydrogels were engineered by mixing normal donor-derived HTM cells with

49   collagen type I, elastin-like polypeptide and hyaluronic acid, each containing photoactive

50   functional groups, followed by UV light-activated free-radical crosslinking. Glaucomatous

51   conditions were induced with dexamethasone (DEX), and therapeutic effects of the Rho-

52   associated kinase (ROCK) inhibitor Y27632 on cytoskeletal organization and tissue-level

53   function, contingent on HTM cell-ECM interactions, were assessed.

54   **Results:** DEX exposure increased HTM hydrogel contractility, f-actin and alpha smooth muscle

55   actin abundance and rearrangement, ECM remodeling, and fibronectin and collagen type IV

56   deposition, all contributing to HTM hydrogel condensation and stiffening consistent with recent

57   data from normal vs. glaucomatous HTM tissue. Y27632 treatment produced precisely the

58   opposite effects and attenuated the DEX-induced pathologic changes, resulting in HTM hydrogel

59   relaxation and softening.

60   **Conclusions:** We have developed a biomimetic HTM hydrogel model for detailed investigation

61   of 3D cell-ECM interactions under normal and simulated glaucomatous conditions. Its

62   bidirectional responsiveness to pharmaceutical challenge and rescue suggests promising potential

63   to serve as screening platform for new POAG treatments with focus on HTM biomechanics.

64 **Introduction**

65 The human trabecular meshwork (HTM), located in the iridocorneal angle, is an avascular

66 connective tissue with filtering features and complex architecture [1]. Its main function is to

67 control the resistance to drainage of aqueous humor (AH) via the conventional outflow pathway

68 to maintain normal intraocular pressure (IOP) [2]. Most of the AH outflow resistance is localized

69 to the deepest juxtacanalicular tissue (JCT) region [3], where a few discontinuous layers of HTM

70 cells reside in and interact with a dense amorphous extracellular matrix (ECM). A variety of

71 ECM structural and organizational components have been identified within the JCT; e.g., non-

72 fibrillar and fibrillar collagens, elastic fibrils, and basement membrane-like materials. The

73 narrow space between HTM cells and ECM fibers is filled with a ground substance rich in

74 proteoglycans and the glycosaminoglycan hyaluronic acid (HA) [3-7].

75

76 HTM cells play an essential role in modulating AH outflow resistance by controlling the

77 production of contraction forces and the secretion/degradation of ECM proteins to support tissue

78 homeostasis [8]. As such, the reciprocity between HTM cells and their ECM is critical for normal

79 tissue function and IOP maintenance within narrow margins in the healthy eye. Dysregulation of

80 HTM cells can cause elevated ECM deposition as well as HTM cell and tissue contraction,

81 which jointly contribute to HTM stiffening, ultimately leading to increased AH outflow

82 resistance and elevated IOP [9,10]. Prolonged elevation of IOP causes pathologic distension and

83 compression of the HTM and further tissue stiffening. Consequently, the stiffened HTM

84 negatively affects IOP and HTM cell function in a feed-forward loop [11-13]. Since elevated IOP is

85 a primary risk factor for glaucoma, this pathologic process leads to retinal ganglion cell damage

86   resulting in the irreversible loss of vision that is characterized as primary open-angle glaucoma

87   (POAG), the most common form of glaucoma [14-18].

88

89   Elevated IOP is the only modifiable risk factor for POAG, and management of the disease is

90   focused on IOP lowering [16]. First line POAG medications do not specifically target the diseased

91   HTM; instead, they lower IOP by either increasing AH outflow bypassing the HTM altogether,

92   or by decreasing AH production [19,20]. In the United States, only the recently approved Rho-

93   associated kinase (ROCK) inhibitor netarsudil [21] directly aims at the stiffened HTM to increase

94   AH outflow via cell/tissue relaxation [22-26]. However, various adverse events at the ocular surface

95   in some patients have been reported during the drug's brief window of availability [27-29], raising

96   concerns over its routine use. This highlights the clear unmet need for new/improved POAG

97   treatment strategies. Targeting ECM mechanics by reversing tissue stiffening to limit

98   pathological progression is an emerging therapeutic approach in other diseases [30], with promising

99   potential for POAG therapy.

100

101   A number of models are available to study HTM physiology and POAG pathophysiology; e.g.,

102   conventional two dimensional (2D) HTM cell monolayer cultures, perfusion-cultured anterior

103   segments from postmortem human and animal eyes, or animal models of different (large and

104   small) species [31-35]. While each of these model systems has proven strengths, they cannot reliably

105   and efficiently determine the relative contributions of HTM cells and their ECM to the onset and

106   progression of glaucomatous HTM stiffening. This has hampered advances in the mechanistic

107   study of this biomechanical element in POAG pathophysiology.

108

109   The interdisciplinary field of tissue engineering aims to produce functional biomimetic replicas

110   of tissues of interest [36]. HTM tissue engineering is still in its infancy; few studies have been

111   reported that use bioengineered 3D HTM *in vitro* models. Constructs made of porous scaffolds

112   (~20 μm thick) seeded with HTM cells were shown to partially mimic normal *in vivo* tissue

113   function, including pharmacological induction/rescue of glaucomatous conditions [37-39]. However,

114   an argument could be made that this model is more akin to a 2D cell culture system (i.e., HTM

115   cells grown on a flat culture substrate) rather than a true 3D model, as it cannot accurately mimic

116   the 3D cell-ECM interface beyond ECM secreted by the HTM cells while grown atop the

117   synthetic polymer scaffold. Another scaffold-based approach utilized porcine TM cells [40] or

118   HTM cells [41] cultured atop a freeze-dried polymer matrix made of collagen and chondroitin

119   sulfate and/or HA exhibiting aligned pores throughout the 3D construct (~3 mm thick). The

120   scaffolds were shown to support TM cell proliferation into the porous matrix, and the

121   bioengineered constructs displayed certain aspects of normal tissue function. Nevertheless, the

122   study did not investigate the constructs' behavior under induced glaucomatous conditions.

123

124   In addition to scaffold-based systems, viscoelastic hydrogels (i.e., water-swollen networks of

125   polymers) are widely used in tissue engineering applications. They provide a simplistic version

126   of the natural 3D tissue environment and allow for accurate *in vitro* modeling of cellular

127   behaviors [42-46]. To that end, Matrigel, the gelatinous protein mixture secreted by mouse sarcoma

128   cells, has been used to fabricate a rudimentary 3D HTM hydrogel culture model [47-49]. Significant

129   drawbacks include Matrigel's tumorigenic origin, diverse composition, and batch-to-batch

130   variability affecting its biochemical and mechanical properties [50]. Lastly, a recent study reported

131   a shear-thinning peptide hydrogel with HTM cells seeded atop to engineer an injectable HTM

132   implant with utility as *in vitro* model [51]. However, this simple 20-residue peptide cannot

133   faithfully recapitulate the complex ECM environment HTM cells interact with in the native

134   tissue. Together, these studies highlight the need for more well-defined hydrogel systems to

135   support relevant HTM modeling studies under normal and induced glaucomatous conditions.

136

137   Here, we report a novel tissue-engineered HTM hydrogel composed of normal donor-derived

138   HTM cells and ECM biopolymers found in the native tissue, with focus on modeling the JCT

139   region owing to both its critical role in regulating AH outflow resistance and IOP, and

140   inextricable link to glaucomatous HTM stiffening. HTM hydrogels in different sizes/shapes were

141   formed by mixing HTM cells with collagen type I, HA, and elastin-like polypeptide (ELP) - each

142   containing photoactive functional groups - followed by photoinitiator-mediated short UV

143   crosslinking. We then used proven pharmacological induction of glaucomatous conditions by

144   treating HTM hydrogels with the corticosteroid dexamethasone (DEX) [35] and assessed the

145   therapeutic effects of the ROCK inhibitor Y27632 [52], either as co- or sequential treatment, on

146   cytoskeletal organization and tissue-level functional changes contingent on HTM cell-ECM

147   interactions. We showed that DEX increased HTM hydrogel contractility, f-actin and alpha

148   smooth muscle actin (αSMA) abundance and rearrangement, ECM remodeling, and fibronectin

149   and collagen type IV deposition, all contributing to HTM hydrogel condensation and stiffening.

150   Y27632 treatment had precisely opposite effects and was shown to prevent or rescue the DEX-

151   induced pathologic changes, resulting in HTM hydrogel relaxation and softening. Together, we

152   have developed a biomimetic HTM hydrogel model that allows for detailed investigation of 3D

153   cell-ECM interactions under normal and simulated glaucomatous conditions. The bidirectional

154   responsiveness of the HTM hydrogel model system to pharmaceutical challenge and rescue

155 suggests promising potential to serve as a screening platform for new POAG treatments with

156 focus on HTM cell/tissue biomechanics.

157   **Materials and Methods**

158   ***HTM cell isolation and culture.*** Human donor eye tissue use was approved by the SUNY

159   Upstate Medical University Institutional Review Board (protocol #2018-0), and all experiments

160   were performed in accordance with the tenets of the Declaration of Helsinki for the use of human

161   tissue. Normal human trabecular meshwork (HTM) cells were isolated from healthy donor

162   corneal rims discarded after transplant surgery, and cultured according to established protocols

163   [53,54]. Using an SMZ1270 stereomicroscope (Nikon Instruments, Melville, NY, USA), corneal

164   rims were cut into wedges and the HTM tissue was grabbed by placing one tip of Dumont #5

165   fine-tipped forceps (Fine Science Tools, Foster City, CA, USA) into the Schlemm's canal lumen

166   and the other on top of the anterior HTM. The dissected strips of HTM tissue were digested for

167   20 min with 1 mg/ml collagenase (Worthington, Lakewood, NJ, USA) and 15 µl/ml human

168   albumin (Sigma-Aldrich, St. Louis, MO, USA) in Dulbecco's Phosphate Buffered Saline (DPBS;

169   Gibco; Thermo Fisher Scientific, Waltham, MA, USA) at 37ºC, placed into a single well of

170   gelatin-coated (Sigma-Aldrich) 6-well culture plates (Corning; Thermo Fisher Scientific), and

171   overlaid with glass coverslips to aid in tissue adherence. HTM tissue strips were cultured in low-

172   glucose Dulbecco's Modified Eagle's Medium (DMEM; Gibco) containing 20% fetal bovine

173   serum   (FBS;   Atlanta   Biologicals,   Flowery   Branch,   GA,   USA)   and   1%

174   penicillin/streptomycin/glutamine (PSG; Gibco), and maintained at 37°C in a humidified

175   atmosphere with 5% CO_2. Fresh media was supplied every 2-3 days. Once confluent, HTM cells

176   were lifted with 0.25% trypsin/0.5 mM EDTA (Gibco) and sub-cultured in DMEM with 10%

177   FBS and 1% PSG. All studies were conducted using cells passage 3-7; the reference HTM cell

178   strain HTM129 was isolated and characterized at Duke University by W.D.S. (Table 1).

179

180

Table 1. HTM cell strain information.

ID	Sex	Age
Reference (HTM129)*	Female	75
HTM01	Female	26
HTM11	Female	47
HTM12	Female	60
*obtained from the Stamer laboratory at Duke University		

181

182   ***HTM cell characterization.*** HTM cells were seeded at 1×10^4 cells/cm^2 in 6-well culture plates or

183   on glass coverslips in 24-well culture plates, and cultured in DMEM with 10% FBS and 1% PSG.

184   HTM cell morphology and growth characteristics were monitored by phase contrast microscopy

185   using an LMI-3000 Series Routine Inverted Microscope (Laxco; Thermo Fisher Scientific). Once

186   confluent, HTM cells were treated with 100 nM dexamethasone (DEX; Fisher Scientific) or

187   vehicle control (0.1% (v/v) ethanol) in DMEM with 1% FBS and 1% PSG for 4 d, and serum-

188   and phenol red-free DMEM for 3 d. The HTM cell culture supernatants were collected and

189   concentrated using Amicon® Ultra Centrifugal Filters (Millipore Sigma, Burlington, MA, USA)

190   for immunoblot analysis. The monolayer HTM cells were processed for quantitative reverse

191   transcription-polymerase chain reaction (qRT-PCR) and immunocytochemistry (ICC) analyses.

192   DEX-induced myocilin (MYOC) upregulation in more than 50% of HTM cells was used as

193   inclusion/exclusion criterion.

194

195   ***Immunoblot analysis.*** Equal protein amounts (10 μg), determined by standard bicinchoninic acid

196   assay (Pierce; Thermo Fisher Scientific), from concentrated HTM cell culture supernatants ±

197   DEX at 7 d supplemented with Halt™ protease/phosphatase inhibitor cocktail (Thermo Fisher

198   Scientific) in 6X loading buffer (Boston Bio Products, Ashland, MA, USA) with 5% beta-

199   mercaptoethanol (BME; Fisher Scientific), were subjected to SDS-PAGE using NuPAGE™ 4-12%

200   Bis-Tris Gels (Invitrogen; Thermo Fisher Scientific) at 200V for 50 min and transferred to 0.45

201   μm PVDF membranes (Millipore; Thermo Fisher Scientific). Membranes were blocked with 5%

202   nonfat milk (Nestlé USA, Glendale, CA, USA) in tris-buffered saline with 0.2% Tween®20

203   (TBST; Thermo Fisher Scientific), and probed with a primary antibody against MYOC (anti-

204   MYOC [MABN866] 1:2000; Sigma-Aldrich) followed by incubation with an HRP-conjugated

205   secondary antibody (Cell Signaling, Danvers, MA, USA). Bound antibodies were visualized with

206   the enhanced chemiluminescent detection system (Pierce) on autoradiography film (Thermo

207   Fisher Scientific).

208

209   ***Quantitative reverse transcription-polymerase chain reaction (qRT-PCR) analysis.*** Total RNA

210   was extracted from HTM cells ± DEX at 7 d (N = 3 per group and donor) using PureLink RNA

211   Mini Kit (Invitrogen). RNA concentration was determined with a NanoDrop spectrophotometer

212   (Thermo Fisher Scientific). RNA was reverse transcribed using iScript™ cDNA Synthesis Kit

213   (BioRad, Hercules, CA, USA). Fifty nanograms of cDNA were amplified in duplicates in each

214   40-cycle reaction using a CFX 384 Real Time PCR System (BioRad) with annealing temperature

215   set at 60ºC, Power SYBR™ Green PCR Master Mix (Thermo Fisher Scientific), and custom-

216   designed qRT-PCR primers for MYOC and Glyceraldehyde 3-phosphate dehydrogenase

217   (GAPDH) (IDT, Coralville, IA, USA; Table 2). Transcript levels were normalized to GAPDH,

218   and DEX-induced MYOC mRNA fold-changes calculated relative to vehicle controls using the

219   comparative C_T method [55].

220

Table 2. qRT-PCR primer information.

Gene	Forward	Reverse
MYOC	ATTCTTGGGGTGGCTACACG	TGATGAAGGCATTGGCGACT
GAPDH	GTCTCCTCTGACTTCAACAGCG	ACCACCCTGTTGCTGTAGCCAA

222

223   ***Immunocytochemistry analysis.*** HTM cells ± DEX at 7 d were fixed with 4% paraformaldehyde

224   (PFA; Thermo Fisher Scientific) at room temperature for 10 min, permeabilized with 0.5%

225   Triton™ X-100 (Thermo Fisher Scientific), blocked with blocking buffer (BioGeneX, Fremont,

226   CA, USA), and incubated with primary antibodies against MYOC (anti-MYOC [ab41552] 1:200;

227   Abcam, Cambridge, MA, USA) or alpha B-Crystallin (anti-CRYAB [ab13497] 1:200; Abcam)

228   followed by incubation with Alexa Fluor® 488-conjugated secondary antibodies (Abcam).

229   Nuclei were counterstained with 4',6'-diamidino-2-phenylindole (DAPI; Abcam). Coverslips

230   were mounted with ProLong™ Gold Antifade (Thermo Fisher Scientific) on Superfrost™ Plus

231   microscope slides (Fisher Scientific), and fluorescent images were acquired with an Eclipse N*i*

232   microscope (Nikon). Four fields of view per sample were analyzed to quantify percent of cells

233   expressing   MYOC,   followed   by   calculation   of   mean   ±   SD   as   follows:

234   DEX-induced MYOC upregulation = $(Mean_{DEX} - Mean_{Ctrl}) \pm [(SD_{DEX})^2 + (SD_{Ctrl})^2]^{1/2}$.

235

236   ***Elastin-like polypeptide (ELP) expression and analysis.*** A plasmid containing an ELP sequence

237   was kindly provided by Dr. Annabi (University of California, Los Angeles). It consists of 70

238   repeats of the pentapeptide VPGVG, in which the 1st valine was replaced with isoleucine in

239   every 5th pentapeptide (i.e., ([VPGVG]$_4$[IPGVG])$_{14}$), flanked by KCTS residues to render the

240   ELP UV-crosslinkable [56]. *Escherichia coli (E. coli)* was used as a host to express the protein as

241   described previously [56,57]. Briefly, a 50 ml *E. coli* starter culture in terrific broth (Thermo Fisher

242   Scientific) was incubated at 37°C overnight, followed by inoculation (1:100) of the expression

243   culture and incubation at 37°C for 24 h. Bacterial pellets were collected and resuspended in lysis

244   buffer (10 mM Tris, 1 mM EDTA, 100 mM NaCl, 5 mM MgCl$_2$, 14.3 mM β-mercaptoethanol

245   (BME); Thermo Fisher Scientific). Lysozyme (Acros Organics, Fair Lawn, NJ, USA) was added

246   to the solution at 1 mg/ml and samples were incubated for 30 min on ice, followed by 5 min

247   sonication (1 min on, 1 min off). The solution was centrifuged at 15,000 g for 20 min at 4°C and

248   the supernatant was kept. To precipitate the protein, 1 M NaCl was added and centrifuged at

249   15,000 g for 20 min at 37°C. ELP was purified using inverse transition cycling (1 cold spin, one

250   hot spin; x3), dialyzed against diH$_2$O at 4°C for 18 h, and lyophilized. For characterization, ELP

251   was reconstituted in DPBS at 10 mg/ml. Ten micrograms of ELP in 6X loading buffer (Boston

252   Bio Products) with 5% BME (Fisher Scientific) were subjected to SDS-PAGE using NuPAGE™

253   10% Bis-Tris Gels (Invitrogen) at 200V for 40 min. Gels were stained with Coomassie Blue R-

254   250 (Biorad) and de-stained in a solution containing 50% (v/v) diH$_2$O, 40% ethanol, and 10%

255   acetic acid (Sigma-Aldrich). De-stained gels were imaged using a ChemiDoc system (BioRad)

256   (**Suppl. Fig. S1**).

257

258   ***Hydrogel precursor solutions.*** Methacrylate-conjugated bovine collagen type I (MA-COL;

259   Advanced BioMatrix, Carlsbad, CA, USA) was reconstituted in sterile 20 mM acetic acid at 6

260   mg/ml. Immediately prior to use, 1 ml MA-COL was neutralized with 85 µl neutralization buffer

261   (Advanced BioMatrix) according to the manufacturer's instructions. Thiol-conjugated hyaluronic

262   acid (SH-HA; Glycosil®; Advanced BioMatrix) was reconstituted in sterile diH$_2$O containing

263   0.5% (w/v) photoinitiator (4-(2-hydroxyethoxy) phenyl-(2-propyl) ketone; Irgacure® 2959;

264   Sigma-Aldrich) at 10 mg/ml according to the manufacturer's protocol. In-house expressed ELP

265   (SH-ELP; thiol via KCTS flanks) was reconstituted in DPBS at 10 mg/ml and sterilized using a

266   0.2 µm syringe filter in the cold.

267

268   ***Preparation of PDMS molds.*** Custom master molds (8-mm diameter x 1-mm depth, or 8-mm

269   diameter x 2-mm depth) were 3D-printed (F170; Stratasys, Eden Prairie, MN, USA) using ABS-

270   M30 filament (Suppl. Fig. S2). Polydimethylsiloxane (PDMS; Sylgard 184, Dow Corning,

271   Midland, MI, USA) was mixed in a 10:1 ratio of elastomer to curing agent according to the

272   manufacturer's protocol, poured into the 3D-printed negative master molds, degassed under

273   vacuum in a desiccator, and cured overnight at 60ºC. The PDMS molds were sterilized under UV

274   light for 30 min prior to use.

275

276   ***Preparation of HTM hydrogels.*** HTM cells (1.0x10^6 cells/ml) were thoroughly mixed with MA-

277   COL (3.6 mg/ml [all final concentrations]), SH-HA (0.5 mg/ml, 0.025% (w/v) photoinitiator),

278   and SH-ELP (2.5 mg/ml) on ice. The HTM cell-laden hydrogel precursor solution was pipetted:

279   a) onto PDMS-coated (Sylgard 184; Dow Corning) 24-well culture plates (10 µl droplets), b)

280   into custom 8x1-mm PDMS molds (50 µl), c) onto 12-mm round glass coverslips (10 µl droplets)

281   followed by spreading with pipette tips, or d) into standard 24-well culture plates (150 µl)

282   depending on the type of experiment, and UV crosslinked (OmniCure S1500 UV Spot Curing

283   System; Excelitas Technologies, Mississauga, Ontario, Canada) at 320-500 nm, 2.2 W/cm^2 for 1-

284   30 s before transferring constructs to 24-well culture plates (**Fig. 1**). One milliliter of DMEM

285   with 10% FBS and 1% PSG was added to each well, and constructs were maintained at 37°C in a

286   humidified atmosphere with 5% CO_2. HTM hydrogels were cultured for 1-10 d with media

287   replenished every 3 d.

288
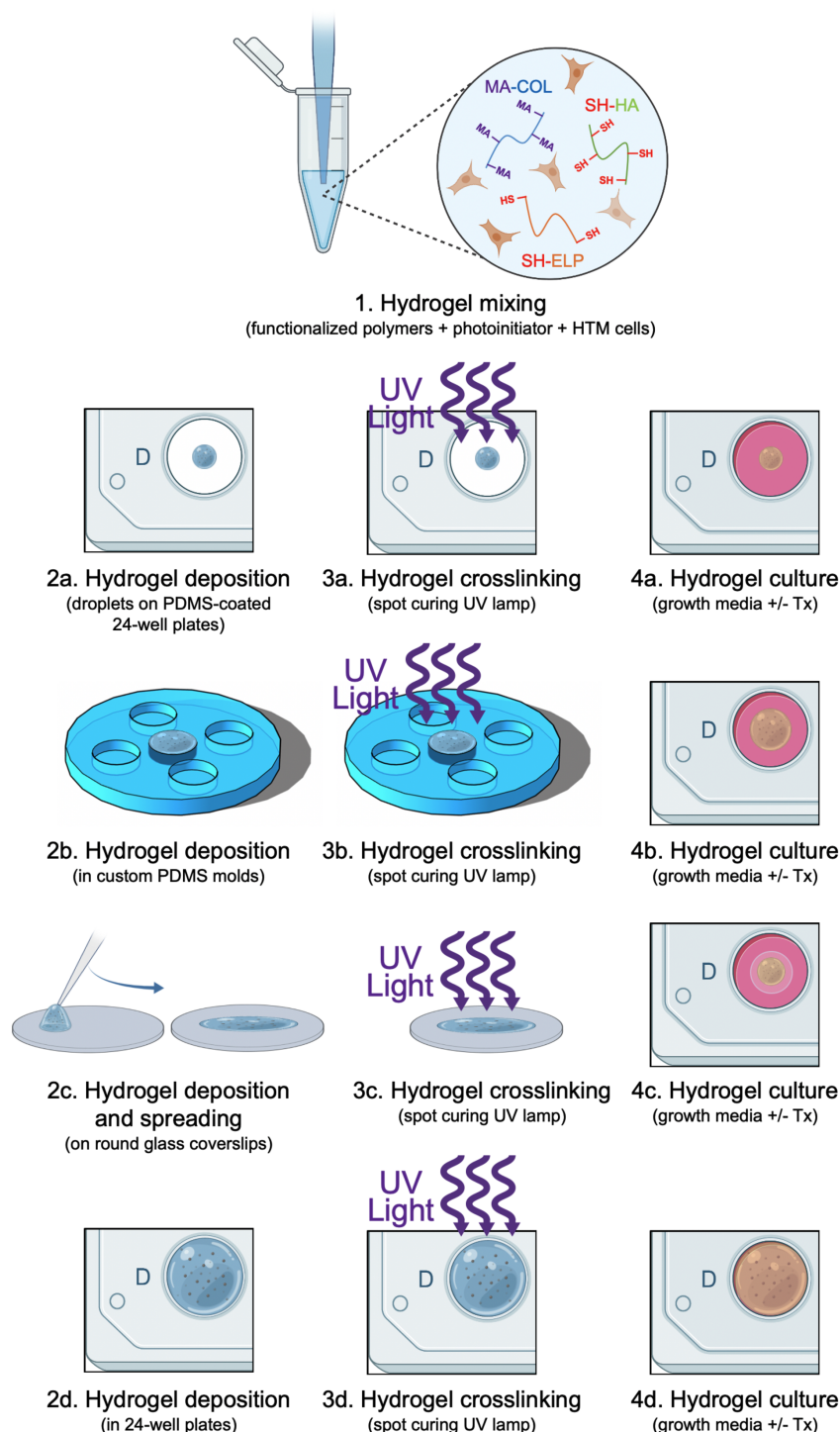
Fig. 1. Schematic of HTM hydrogel formation. HTM hydrogels were fabricated by mixing HTM cells (1×10^6 cells/ml) with methacrylate-conjugated collagen type I (MA-COL), thiol-conjugated hyaluronic acid (SH-HA; with photoinitiator), and in-house expressed elastin-like polypeptide (SH-ELP; thiol via KCTS flanks). Desired volumes of the HTM cell-laden hydrogel precursor solutions were added to different wells/molds [a] 10 µl on PDMS-coated 24-well

295   plates, b) 50 µl in custom 8x1-mm PDMS molds, c) 10 µl on glass coverslips + spreading, d) 150
296   µl in standard 24-well culture plates], UV crosslinked (320-500 nm, 2.2 W/cm^2, 1-30 s), and
297   cultured in growth media, without or with different treatments, for 1-10 d.

298

299   ***HTM hydrogel microstructural analysis.*** One hundred microliters of acellular hydrogel

300   precursor solutions were pipetted into custom 8x2-mm PDMS molds, made from 3D-printed

301   templates, UV crosslinked, and equilibrated in DPBS for 3 h to wash off any un-crosslinked

302   polymers. Hydrogel samples were bisected to expose the interior hydrogel network surface and

303   fixed in 4% PFA at 4°C overnight, washed with DPBS, flash frozen in liquid nitrogen, and

304   lyophilized. Dried samples were mounted on scanning electron microscopy (SEM) stubs, sputter

305   coated with gold, and visualized using a JSM-IT100 InTouchScope™ SEM (JEOL USA,

306   Peabody, MA, USA) at 7 kV. Two fields of view per sample were analyzed to quantify hydrogel

307   pore size (N = 40 total) using ImageJ software (National Institutes of Health, Bethesda, MD,

308   USA).

309

310   ***HTM hydrogel cell viability analysis.*** Cell viability was determined using a LIVE/DEAD™

311   Viability/Cytotoxicity Kit (i.e., live = green-stained, dead = red-stained) (Invitrogen) according

312   to the manufacturer's instructions. HTM hydrogels were incubated with the staining solutions

313   (calcein-AM (0.5 µl/ml) and ethidium homodimer-1 (2 µl/ml) in DMEM with 10% FBS and 1%

314   PSG) at 37°C for 45 min and washed with DPBS. Fluorescent images were acquired on 0 d (i.e.,

315   immediately after UV crosslinking; N = 4 per group and donor) and 7 d (qualitative) with an

316   Eclipse T*i* microscope (Nikon). Four fields of view per sample were analyzed to quantify percent

317   HTM cell viability (i.e., ratio of live to total cells), followed by calculation of mean ± SD.

318

319   ***HTM hydrogel cell proliferation analysis.*** Cell proliferation was measured with the CellTiter

320   96® AQueous Non-Radioactive Cell Proliferation Assay (Promega, Madison, WI, USA)

321   following the manufacturer's protocol. HTM hydrogels cultured in DMEM with 10% FBS and 1%

322   PSG for 1-10 d (N = 3 per group and donor) were incubated with the staining solution (38 μl

323   MTS, 2 μl PMS solution, 200 μl DMEM) at 37°C for 1.5 h. Absorbance at 490 nm was recorded

324   using a spectrophotometer plate reader (BioTEK, Winooski, VT, USA). Blank-subtracted

325   absorbance values served as a direct measure of HTM cell proliferation over time.

326

327   ***HTM hydrogel treatments.*** HTM hydrogels cultured in DMEM with 10% FBS and 1% PSG

328   were subjected to the following treatments for 10 d: 1) vehicle control (ethanol; 0.1% (v/v)), 2)

329   DEX (100 nM), 3) Rho-associated kinase (ROCK) inhibitor Y27632 (10 μM; Sigma-Aldrich), 4)

330   DEX (100 nM) + Y27632 (10 μM) [co-treatment], or 5) DEX (100 nM) for 5 d followed by

331   Y27632 (10 μM) for 5 d [sequential-treatment]. To validate our model, HTM hydrogels were

332   subjected to: 1) vehicle control (4 mM hydrochloric acid with 0.1% bovine serum albumin

333   (BSA); Fisher Scientific), 2) transforming growth factor beta-2 (TGF-β2; 2.5 ng/ml; R&D

334   Systems, Minneapolis, MN, USA), 3) latrunculin-b (Lat-B; 2 μM; Fisher Scientific), 4) TGF-β2

335   (2.5 ng/ml) + Lat-B (2 μM) [co-treatment], or 5) TGF-β2 (2.5 ng/ml) for 5 d followed by Lat-B

336   (2 μM) for 5 d [sequential-treatment].

337

338   ***HTM hydrogel contraction analysis.*** HTM hydrogels were cultured in DMEM with 10% FBS

339   and 1% PSG, in absence or presence of the different treatments (N = 3-4 per group and donor; 3

340   independent experiments). Longitudinal brightfield images were acquired over 10 d with an

341   Eclipse T*i* microscope (Nikon). Construct area was measured using ImageJ software (NIH) over

342   time and normalized to 0 d.

343

344   ***HTM hydrogel immunocytochemistry analysis.*** HTM hydrogels, spread on glass coverslips and

345   cultured in DMEM with 10% FBS and 1% PSG in presence of the different treatments for 10 d,

346   were fixed with 4% PFA at 4ºC overnight, permeabilized with 0.5% Triton™ X-100 (Thermo

347   Fisher Scientific), blocked with blocking buffer (BioGeneX), and incubated with primary

348   antibodies against α-smooth muscle actin (anti-αSMA [ab5694] 1:200; Abcam), followed by

349   incubation with an Alexa Fluor® 488-conjugated secondary antibody; nuclei were

350   counterstained with DAPI (both Abcam). Similarly, constructs were stained with Phalloidin-

351   iFluor 488 (Abcam), nuclei were counterstained with DAPI, according to the manufacturer's

352   instructions. Coverslips were transferred to 35-mm glass bottom dishes (MatTek, Ashland, MA,

353   USA), and fluorescent images were acquired with an Eclipse N*i* or T*i* microscope (Nikon).

354

355   ***HTM hydrogel histology and immunohistochemistry analyses.*** HTM hydrogels, cultured in

356   DMEM with 10% FBS and 1% PSG in presence of the different treatments for 10 d were fixed in

357   4% PFA at 4°C overnight, followed by incubation in 30% sucrose for 24 h at 4°C, washed with

358   DPBS, embedded in Tissue-Plus™ O.C.T. Compound (Fisher Scientific), and flash frozen in

359   liquid nitrogen. Twenty micrometer cryosections were cut using a cryostat (Leica Biosystems

360   Inc., Buffalo Grove, IL, USA) and collected on Superfrost™ Plus microscope slides (Fisher

361   Scientific). Sections were stained with picrosirius red/hematoxylin using the Picrosirius Red

362   Stain Kit (PolySciences, Warrington, PA, USA) following the manufacturer's protocol. Slides

363   were mounted with Permount™ (Fisher Scientific) and brightfield images were captured with an

364   Eclipse E400 microscope (Nikon). For immunohistochemistry analyses, sections were

365   permeabilized with 0.5% Triton™ X-100, blocked with blocking buffer, and incubated with

366   primary antibodies against fibronectin (anti-fibronectin [ab45688] 1:500; Abcam) or collagen

367   type IV (anti-collagen IV [ab6586] 1:500; Abcam) followed by incubation with an Alexa Fluor®

368   488-conjugated secondary antibody; nuclei were counterstained with DAPI (both Abcam). Slides

369   were mounted with ProLong™ Gold Antifade (Thermo Fisher Scientific), and fluorescent

370   images were acquired with an Eclipse N*i* microscope (Nikon). Three fields of view per sample

371   were analyzed to quantify normalized fibronectin signal intensity, followed by calculation of

372   fold-change vs. control.

373

374   ***HTM hydrogel rheology analysis.*** Fifty microliters of HTM cell-laden or acellular hydrogel

375   precursor solutions were pipetted into custom 8x1-mm PDMS molds (**Suppl. Fig. S2**). Similarly,

376   150 µl of HTM cell-laden hydrogel precursor solutions were pipetted into 24-well culture plates.

377   All samples were UV crosslinked and equilibrated as described above. Acellular hydrogels were

378   measured on 0 d. HTM hydrogels, cultured in DMEM with 10% FBS and 1% PSG in presence

379   of the different treatments, were measured on 0 d and 10 d; plates were scanned for visualization

380   followed by cutting samples to size using an 8-mm diameter tissue punch. A Kinexus rheometer

381   (Malvern Panalytical, Westborough, MA, USA) fitted with an 8-mm diameter parallel plate was

382   used to measure hydrogel viscoelasticity. To ensure standard conditions across all experiments

383   (N = 3 per group), the geometry was lowered into the hydrogels until a calibration normal force

384   of 0.02 N was achieved. Subsequently, an oscillatory shear-strain sweep test (0.1-60%, 1.0 Hz,

385   25°C) was applied to determine storage modulus (G') and loss modulus (G") in the linear region.

386   Compression testing was performed at axial strains from 0% to -50% by changing the gap

387   between the plates followed by applying a sinusoidal shear strain of 2% at a frequency of 1.0 Hz

388   to determine storage modulus (G') with increasing axial strain.

389

390   ***Statistical analysis.*** Individual sample sizes and details of statistical analyses are specified in

391   each figure caption. Comparisons between groups were assessed by unpaired *t* test, one-way or

392   two-way analysis of variance (ANOVA) with Tukey's multiple comparisons *post hoc* tests, as

393   appropriate. All data are shown with mean ± SD, some with individual data points. The

394   significance level was set at p<0.05 or lower. GraphPad Prism software v8.4 (GraphPad

395   Software, La Jolla, CA, USA) was used for all analyses.

396

397

398   **Results**

399   ***HTM cell characterization***

400   A reliable feature of HTM cells *in vitro* is upregulation of MYOC expression in more than 50%

401   of cells in response to challenge with the corticosteroid DEX [54]. Three strains (HTM01, HTM11,

402   HTM12) were used and compared to a validated reference strain (HTM129). Both HTM01 and

403   HTM12 exhibited normal morphology (i.e., cobblestone-like pattern with some overlapping

404   processes; **Fig. 2A**) and growth characteristics (i.e., contact inhibited with doubling time of ~2 d)

405   comparable to the reference standard. HTM11 showed overall normal morphology; however, a

406   fraction of cells was noticeably larger. An overall slower doubling time (~4 d) was also noted.

407   Significantly increased MYOC mRNA expression by qRT-PCR was observed with DEX

408   treatment vs. controls across HTM cell strains (**Fig. 2B**). Qualitative assessment of secreted

409   MYOC protein by immunoblot showed robust DEX-inducible expression (**Fig. 2C**). Intracellular

410   MYOC expression by immunocytochemistry was increased by 57.9 ± 7.2% (reference), 81.5 ±

411   1.9% (HTM01), 41.5 ± 11.4% (HTM11), and 51.8 ± 6.6% (HTM12) with DEX treatment vs.

412   controls (p<0.001 for all HTM cell strains; **Fig. 2D**). Alpha B-Crystallin (CRYAB) is

413   exclusively expressed in the JCT region of the HTM [58]. Collagenase was used to digest the

414   dissected strips of HTM tissue; specifically, to disrupt contacts between JCT-HTM cells and

415   their dense ECM, and to encourage cell migration out of the HTM tissue. Our results showed that

416   all of our HTM cell strains and the reference cells highly expressed CRYAB (**Fig. 2E**),

417   suggesting that a significant population of cells were derived from the JCT layer. Based on

418   suboptimal cellular morphology and growth characteristics, as well as DEX-inducible

419   intracellular MYOC expression below the threshold of 50%, HTM11 cells were ruled out for the

420   rest of the studies.

421   Together, this data suggests that HTM01 and HTM12 exhibit all required key characteristics

422   according to a recent consensus paper [54] to faithfully identify them as normal HTM cells,

423   comparable to a confirmed reference standard.

424

425
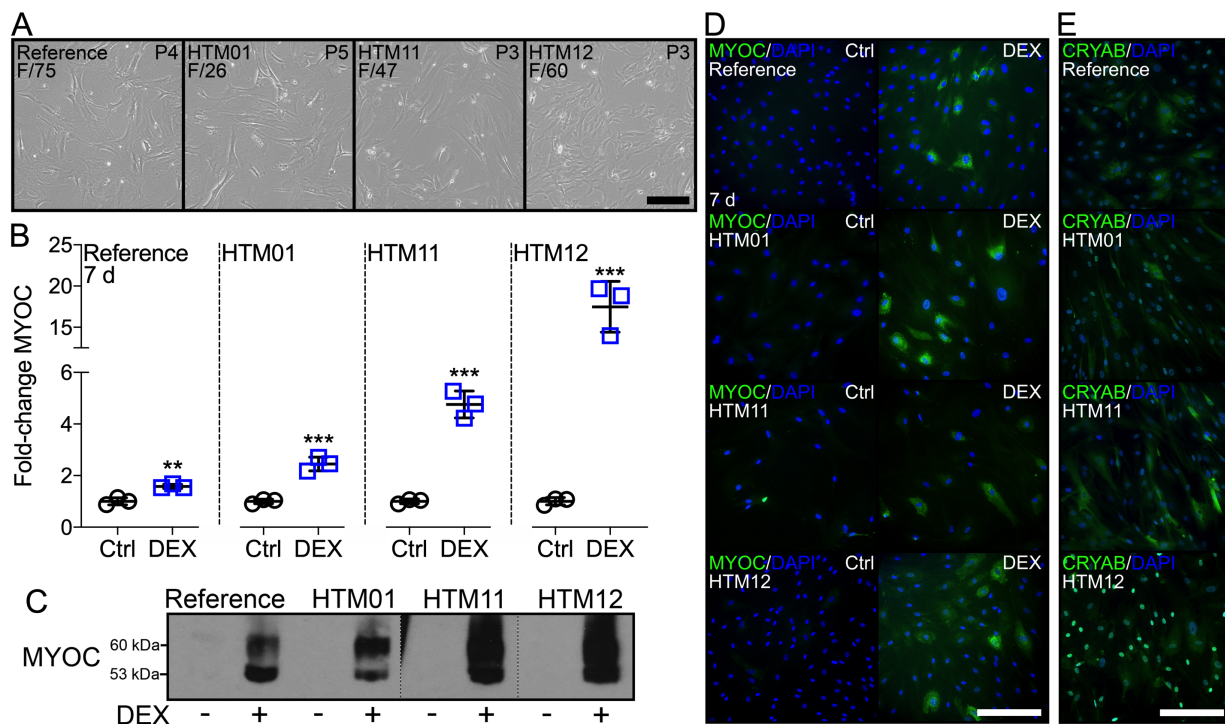
426   **Fig. 2. HTM cell characterization.** (**A**) Representative phase contrast micrographs of reference,
427   HTM01, HTM11, and HTM12 cell strains with sex/age information. Scale bar, 250 µm. (**B**)
428   mRNA fold-change of MYOC by qRT-PCR at 7 d (N = 3 per group and donor; *p<0.05,
429   ***p<0.001 vs. control). (**C**) Immunoblot of secreted MYOC at 7 d. (**D**) Representative
430   fluorescence micrographs of intracellular MYOC at 7 d (MYOC = green; DAPI = blue). Scale
431   bar, 250 µm. (**E**) Representative fluorescence micrographs of CRYAB (CRYAB = green; DAPI
432   = blue). Scale bar, 250 µm.

433

434   *HTM cell viability in hydrogels*

435   The number of HTM cells in native tissue decreases with aging. A steady decline from (0.59-

436   1.74)x10^6 cells/ml in 20-year-old individuals to (0.31-0.92)x10^6 cells/ml in 80-year-old

437   individuals has been shown [7,59]. Therefore, we used a normalized density of $1.0x10^6$ cells/ml in

438   HTM cell-laden hydrogels independent of donor age. To ascertain that HTM cells could

439   withstand the UV light-activated free-radical crosslinking process, referred to as

440   photocrosslinking or UV crosslinking throughout, HTM cell viability in hydrogels crosslinked

441   for increasing times was determined by live/dead staining. Hydrogel-encapsulated HTM cells

442   displayed high viability immediately after photocrosslinking (0 d). We observed negligible cell

443   death across HTM cell strains after 1 s and 5 s of UV crosslinking, and more than 80% cells

444   remained viable after 10 s and 20 s of irradiation. In contrast, significant cell death was noted

445   after 30 s of UV crosslinking (**Fig. 3**).

446   This suggests that UV irradiation for 1-10 s does not cause major cytotoxicity to HTM cells

447   encapsulated in 3D biopolymer hydrogels, regardless of donor age and cell source. Therefore, we

448   focused on HTM01 and HTM12 isolated in our laboratory for subsequent experiments.

449

450
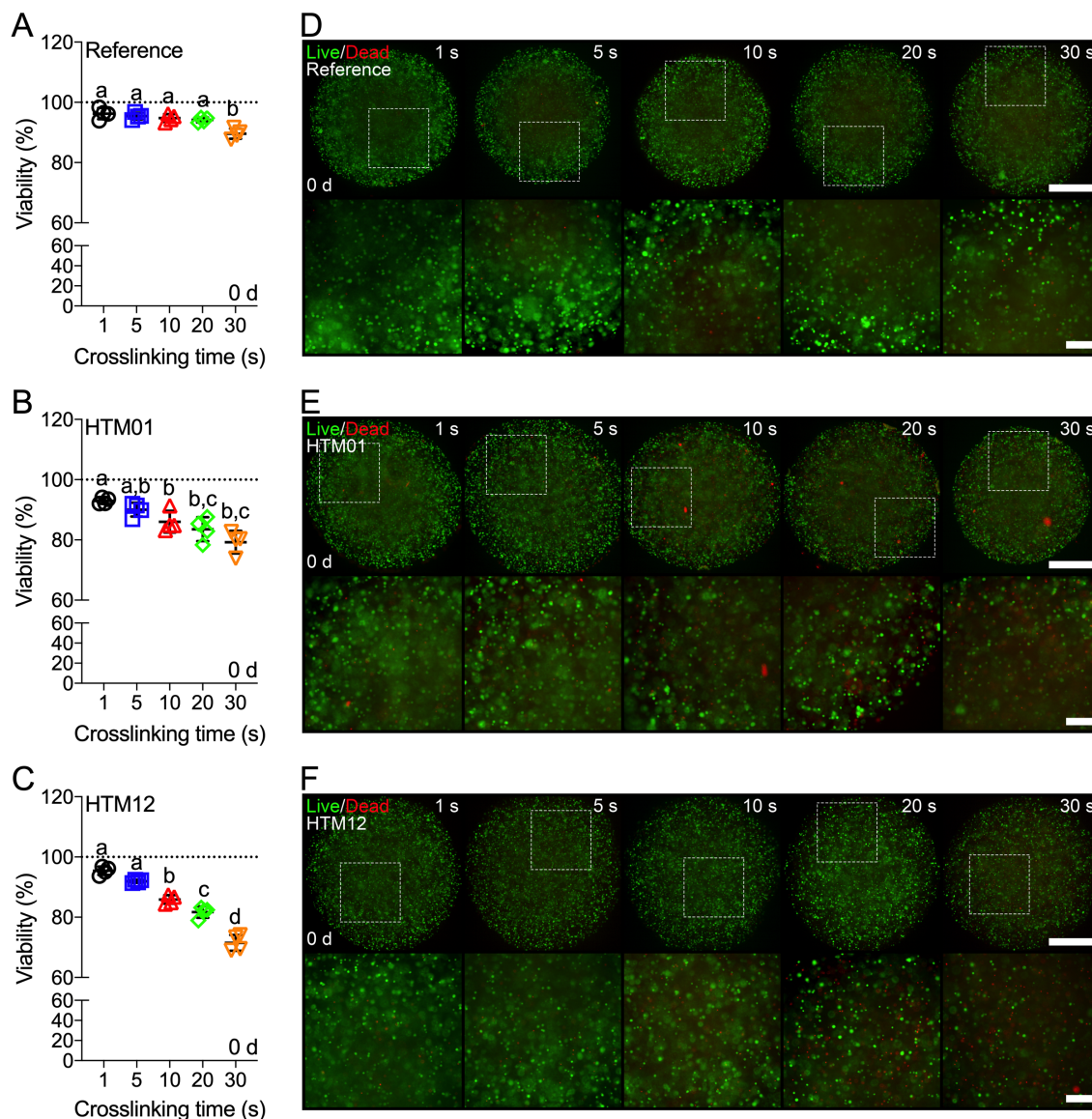
Fig. 3. HTM cell viability. Cell viability quantification of hydrogel-encapsulated (**A**) reference, (**B**) HTM01, and (**C**) HTM12 cells across UV crosslinking times at 0 d (N=4 per group and donor; dotted lines show 100% viability for reference; shared significance indicator letters represent non-significant difference (p>0.05), distinct letters represent significant difference (p<0.05)). Representative fluorescence micrographs of (**D**) reference, (**E**) HTM01, and (**F**) HTM12 hydrogels at 0 d (live cells = green; dead cells = red). Scale bars, 1 mm (top) and 250 μm (bottom).

461 ***HTM cell contractility and proliferation in hydrogels***

462 HTM cells interact with and contract their ECM environment [10]. For both HTM01 and HTM12

463 cell strains, an inverse relationship between UV crosslinking time and hydrogel contraction was

464 observed; i.e., constructs showed overall decreased contraction with increasing UV crosslinking

465 time (**Fig. 4; Suppl. Fig. S3**). This was consistent with hydrogel stiffness; i.e., acellular

466 constructs exhibited increased shear storage moduli (G') by rheology with increasing UV

467 crosslinking time, while loss moduli (G") remained relatively stable (**Suppl. Fig. S4**). A key

468 advantage of using hydrogel microenvironments to assess cellular behaviors vs. traditional 2D or

469 scaffold-based 3D culture systems is their viscoelastic behavior [50]. In this study, hydrogels

470 showed tissue-like viscoelastic properties independent of UV crosslinking time, with

471 significantly higher G' vs. G" indicating predominantly elastic rather than viscous characteristics

472 (**Suppl. Fig. S4**).

473 HTM01 hydrogels crosslinked for 1-10 s significantly contracted over culture time, reaching

474 ~40-50% of their original size by 7 d. No differences between constructs irradiated for 1 s and 5

475 s were found, but hydrogels formed after 10 s UV crosslinking were significantly less contracted

476 in comparison (**Fig. 4A,B; Suppl. Fig. S3A**). Constructs in the 20 s group also displayed

477 significant longitudinal contraction, approximating ~80% of their baseline size by 7 d at which

478 point they were significantly less contracted vs. all shorter UV crosslinking groups. HTM01

479 hydrogels crosslinked for 30 s displayed consistent size over time, and were significantly less

480 contracted vs. all other groups at 7 d (**Fig. 4A,B; Suppl. Fig. S3A**). HTM12 hydrogels showed

481 similar overall behavior to HTM01 (**Fig. 4C,D; Suppl. Fig. S3B**). Of note, constructs UV

482 crosslinked for 1 s were significantly more contracted compared to all other groups by 7 d,

483 reaching ~20% of their original size. No differences between constructs irradiated for 20 s and

484   30 s were found; hydrogels were significantly less contracted vs. all shorter UV crosslinking

485   groups (**Fig. 4C,D; Suppl. Fig. S3B**). This data suggests that HTM cells are able to contract and

486   deform the hydrogels photocrosslinked for 1-10 s independent of cell strain.

487   Taken together, consistent hydrogel formation was observed with 5 s UV crosslinking. Using

488   these conditions, constructs showed high HTM cell viability immediately after hydrogel

489   formation (**Fig. 3**) together with reliable contractile-mediated hydrogel deformation over time

490   (**Fig. 4; Suppl. Fig. S3**). This was accompanied by significant HTM cell proliferation in

491   hydrogels over 7 d (**Fig. 5A,B**), at which point negligible cell death and prominent cell spreading

492   were observed with both HTM cell strains (**Fig. 5C**). Therefore, 5 s UV crosslinking time was

493   chosen for all following experiments with focus on HTM12.

494

495
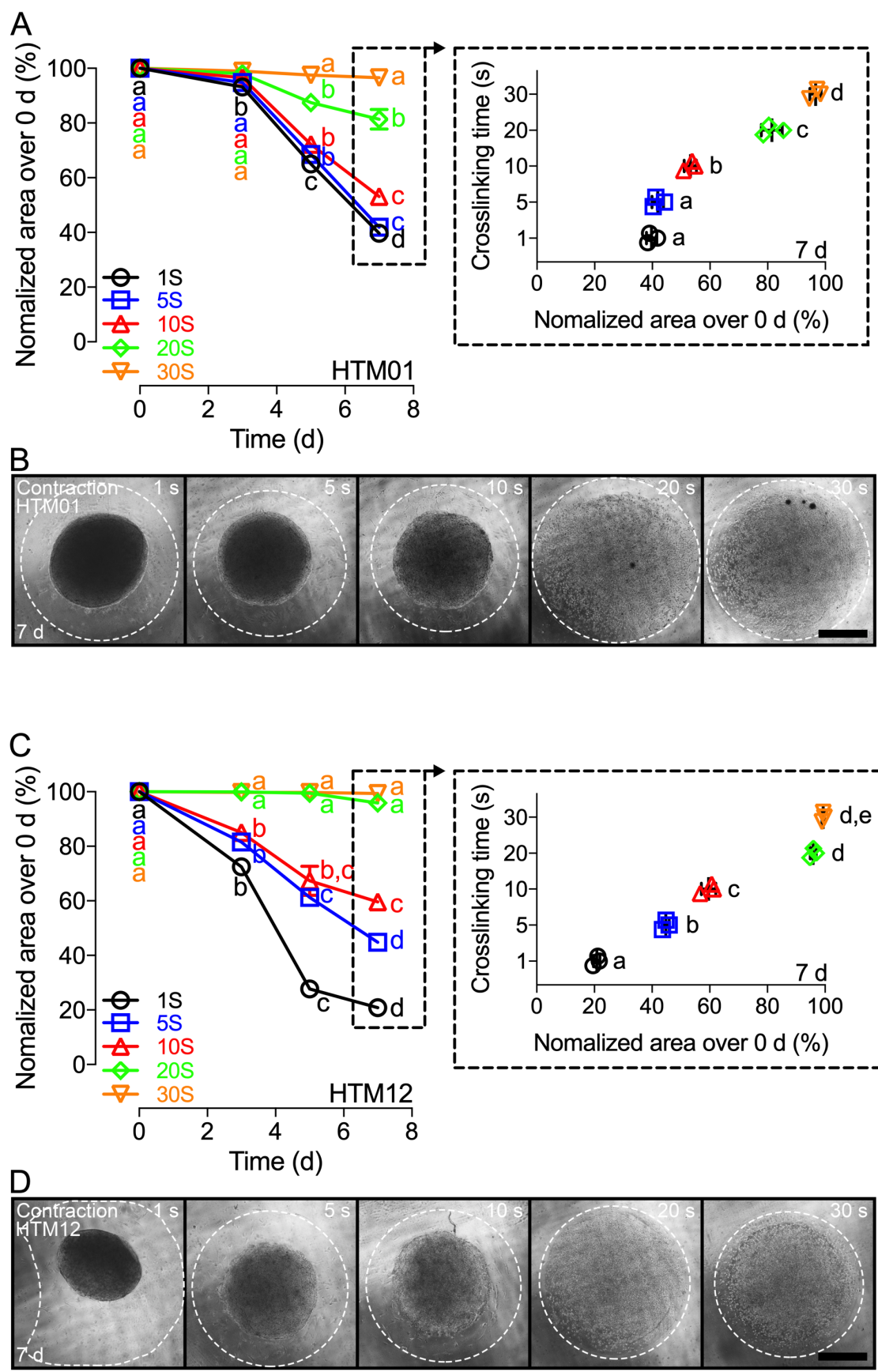
Fig. 4. HTM hydrogel contractility. Longitudinal quantification (i.e., construct size relative to 0 d) of (**A**) HTM01 and (**C**) HTM12 cell contractility in hydrogels across crosslinking times; dashed boxes show detailed comparisons between groups at 7 d (N=3 per group and donor; shared significance indicator letters represent non-significant difference (p>0.05), distinct letters represent significant difference (p<0.05)). Representative brightfield images of (**B**) HTM01 and (**D**) HTM12 hydrogels at 7 d; white dashed lines outline original size of constructs at 0 d. Scale bars, 1 mm.
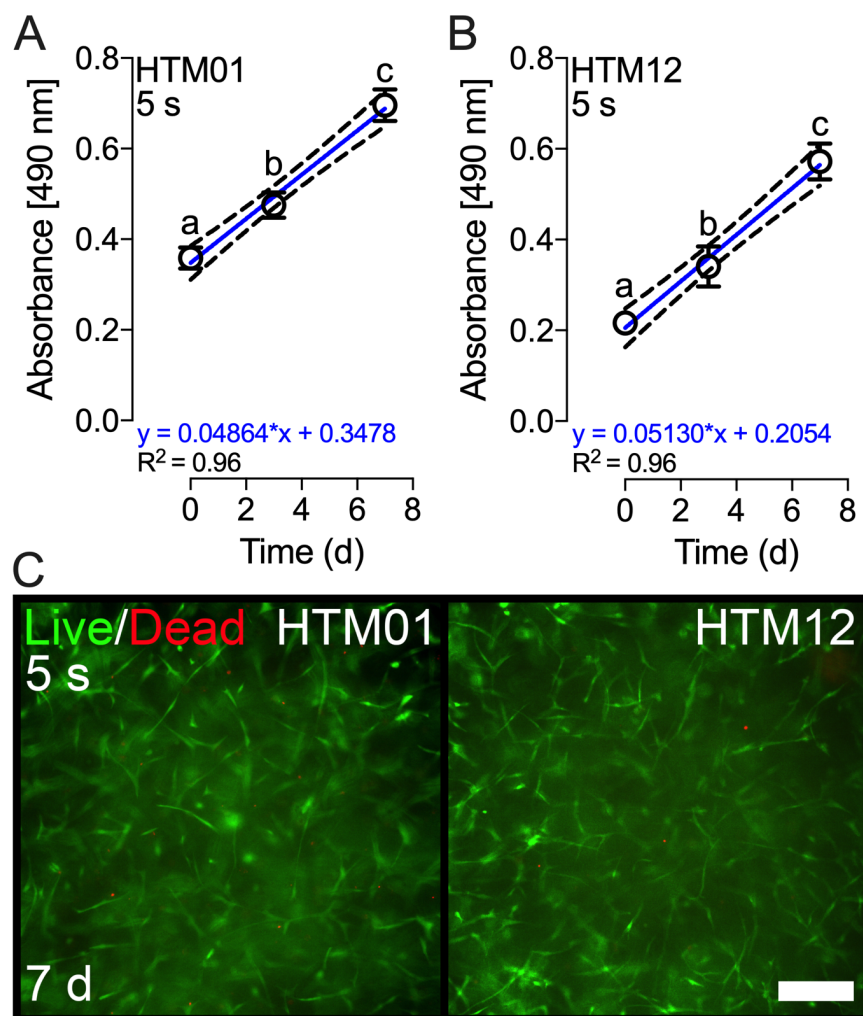
Fig. 5. HTM cell proliferation and viability in hydrogels. Longitudinal cell proliferation quantification of (**A**) HTM01 and (**B**) HTM12 hydrogels crosslinked for 5 s (N=3 per group and donor; shared significance indicator letters represent non-significant difference (p>0.05), distinct letters represent significant difference (p<0.05)). (**C**) Representative fluorescence micrographs of HTM01 and HTM12 hydrogels crosslinked for 5 s at 7 d (live cells = green; dead cells = red). Scale bar, 250 μm.

513   *HTM hydrogel microstructural and mechanical properties*

514   HTM cells within the JCT region reside in a loose connective tissue comprised of reticular and

515   elastic fibers, and ground substance made of proteoglycans and glycosaminoglycans. Pore sizes

516   across the JCT have been estimated at ~2-15 μm [3-7]. To assess the hydrogel microarchitecture,

517   SEM images were acquired on 0 d (i.e., immediately after 5 s UV crosslinking). Acellular

518   hydrogels exhibited a honeycomb-like architecture with 43.3 ± 27.3 μm pore size (**Fig. 6A**),

519   comparable to a recently reported hydrogel made of ELP and HA [57]. For correlative analyses, we

520   next assessed hydrogel mechanical properties by rheology of both acellular and HTM12 cell-

521   encapsulated hydrogels. In general, hydrogel stiffness is dependent on biopolymer

522   concentrations/arrangement and crosslinking density, with encapsulated contractile cells further

523   contributing to construct elasticity. At the chosen crosslinking time of 5 s, we observed overall

524   relatively low modulus values in the low pascal-range, consistent with the low-to-medium

525   biopolymer concentrations used. HTM cell-encapsulated hydrogels were significantly stiffer

526   compared to acellular samples (G', ~75 Pa vs. 47 Pa), while G" was comparable (**Fig. 6B**).

527   Regardless of whether or not cells were present within the 3D biopolymer network, hydrogels

528   displayed tissue-like compression stiffening [60] (i.e., increase in shear modulus with increasing

529   compressive strain) (**Fig. 6C**).

530   This data suggests that our HTM hydrogel system provides an adequately porous and soft 3D

531   microenvironment that mimics the mechanical properties of native heterogeneous soft

532   connective tissues.

533
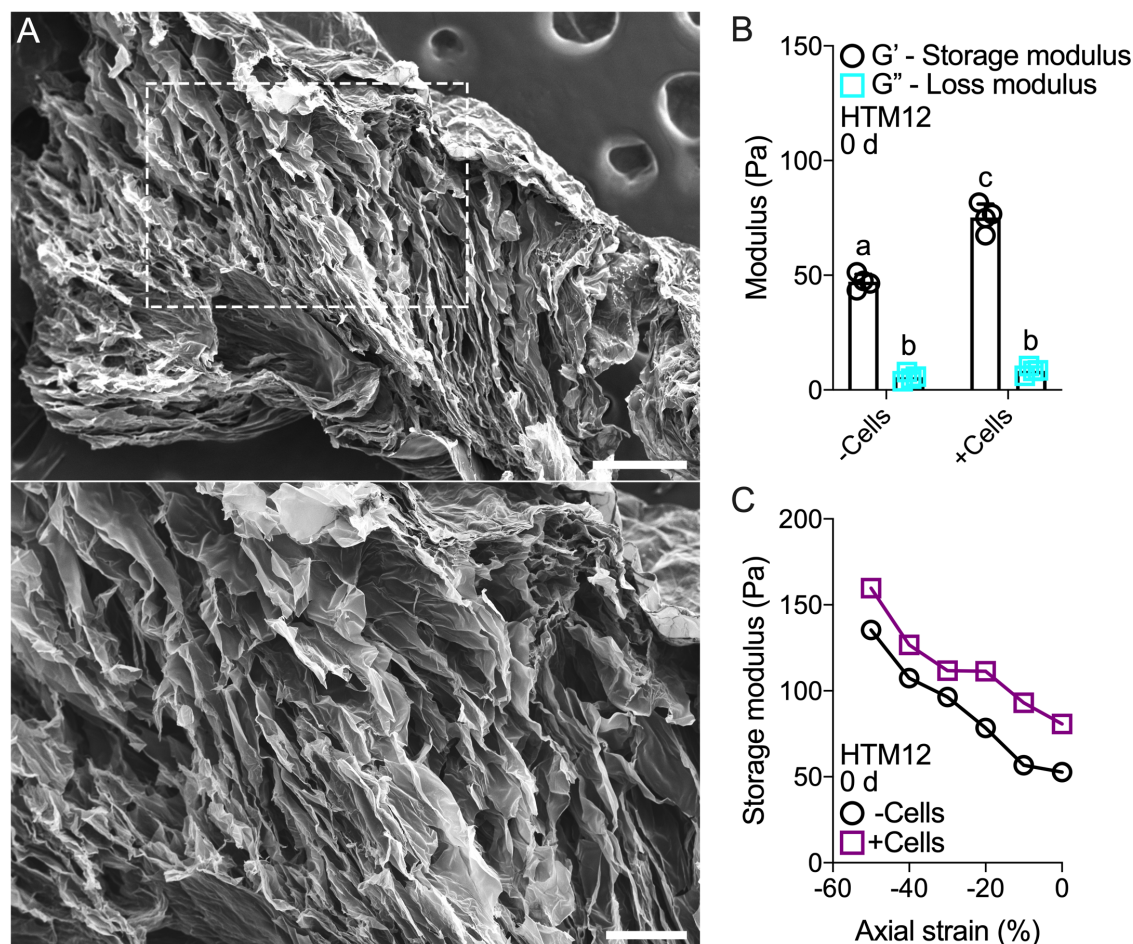
Fig. 6. HTM hydrogel microstructural and mechanical analyses. (**A**) Scanning electron micrographs of acellular hydrogels crosslinked for 5 s at 0 d (dashed box shows region of interest in higher magnification image). Scale bars, 250 μm (top) and 100 μm (bottom). (**B**) Storage and loss moduli of acellular and HTM12 cell-encapsulated hydrogels crosslinked for 5 s at 0 d (N=4 per group; shared significance indicator letters represent non-significant difference (p>0.05), distinct letters represent significant difference (p<0.05)). (**C**) Storage modulus measured at 2% shear strain as a function of axial strain for acellular and HTM12 cell-encapsulated hydrogels crosslinked for 5 s at 0 d (N=1 per group).

HTM cell-laden hydrogels as glaucoma disease model: pharmacological induction/rescue

Hydrogel contractility

The contractility status of HTM cells and overall tissue influences AH outflow resistance and

IOP [61]. Increased HTM contraction is observed in patients with POAG, which typically leads to

548   tissue stiffening, decreased AH outflow facility, and elevated IOP [59]. Steroid therapy is widely

549   used to treat a variety of inflammatory diseases and conditions. However, long term use of ocular

550   corticosteroids such as DEX often results in elevated IOP and POAG [62]. To ascertain whether

551   photocrosslinked HTM hydrogels could serve as a glaucoma disease model, we treated

552   constructs with DEX [54] to induce POAG-like conditions and evaluated its effects on hydrogel

553   contractility. In the United States, the ROCK inhibitor netarsudil is a clinically available drug

554   that directly targets the stiffened HTM to increase AH outflow via cell/tissue relaxation [21-25].

555   Therefore, we assessed the therapeutic effects of ROCK inhibitor Y27632 treatment on HTM

556   hydrogel contractility following DEX induction.

557   We observed significant contraction over time in all groups (**Fig. 7A; Suppl. Fig. S5**). DEX-

558   treated HTM hydrogels exhibited significantly greater contraction vs. controls by 5 d, reaching

559   ~44% of their original size. Comparable values were found in the sequential treatment samples

560   (DEX (5 d) + Y27632 (5 d)), which at this point had only been exposed to DEX rendering the

561   two groups virtually identical. In contrast, Y27632 significantly relaxed the HTM hydrogels (i.e.,

562   decreased contraction; ~70% of their original size) vs. controls. No differences were noted

563   between DEX + Y27632 co-treated samples and controls by 5 d, displaying significantly less

564   contraction compared to DEX- and DEX (5 d) + Y27632 (5 d)-treated HTM hydrogels, yet

565   significantly more contraction vs. Y27632-treated constructs; this suggests that Y27632 can

566   prevent DEX-induced pathologic contraction of HTM hydrogels when presented together (**Fig.**

567   **7A,B,D; Suppl. Fig. S5**).

568   Overall similar trends were observed at 10 d (**Fig. 7A,C,E; Suppl. Fig. S5**). DEX treatment

569   induced significantly more contraction (~26% of their original size), whereas Y27632 treatment

570   resulted in significantly less contraction (~48% of their original size) vs. all other groups. No

571   differences were observed between DEX + Y27632 co-treatment and controls. Importantly, in a

572   clinical scenario, the HTM tissue would likely already show signs of dysfunction before any

573   POAG treatment would be administered. We simulated this with the sequential treatment group:

574   DEX induction for 5 d followed by Y27632 treatment for 5 d with DEX withheld. Our results

575   showed that Y27632 rescued HTM hydrogel contraction induced by DEX and prevented further

576   contraction; i.e., construct size with DEX (5 d) + Y27632 (5 d) sequential treatment was similar

577   to the control and DEX + Y27632 groups, but significantly increased compared to DEX-treated

578   samples (**Fig. 7A,C,E; Suppl. Fig. S5**).

579   Next, to see if hydrogel contractility was influenced by the cell number,   we assessed HTM cell

580   proliferation in constructs subjected to the different treatments. Significant HTM cell

581   proliferation over time was observed in all groups (**Fig. 7F).** No differences between groups

582   were found at 5 d; however, by 10 d HTM cells in the DEX-treated group showed significantly

583   less proliferation compared to the Y27632 treated group (**Fig. 7F; inset in dashed box**).

584   Together, this suggests that DEX robustly induces HTM hydrogel contractility mimicking

585   glaucomatous conditions, and that ROCK inhibition prevents or rescues DEX-induced

586   pathologic contraction.

587

588
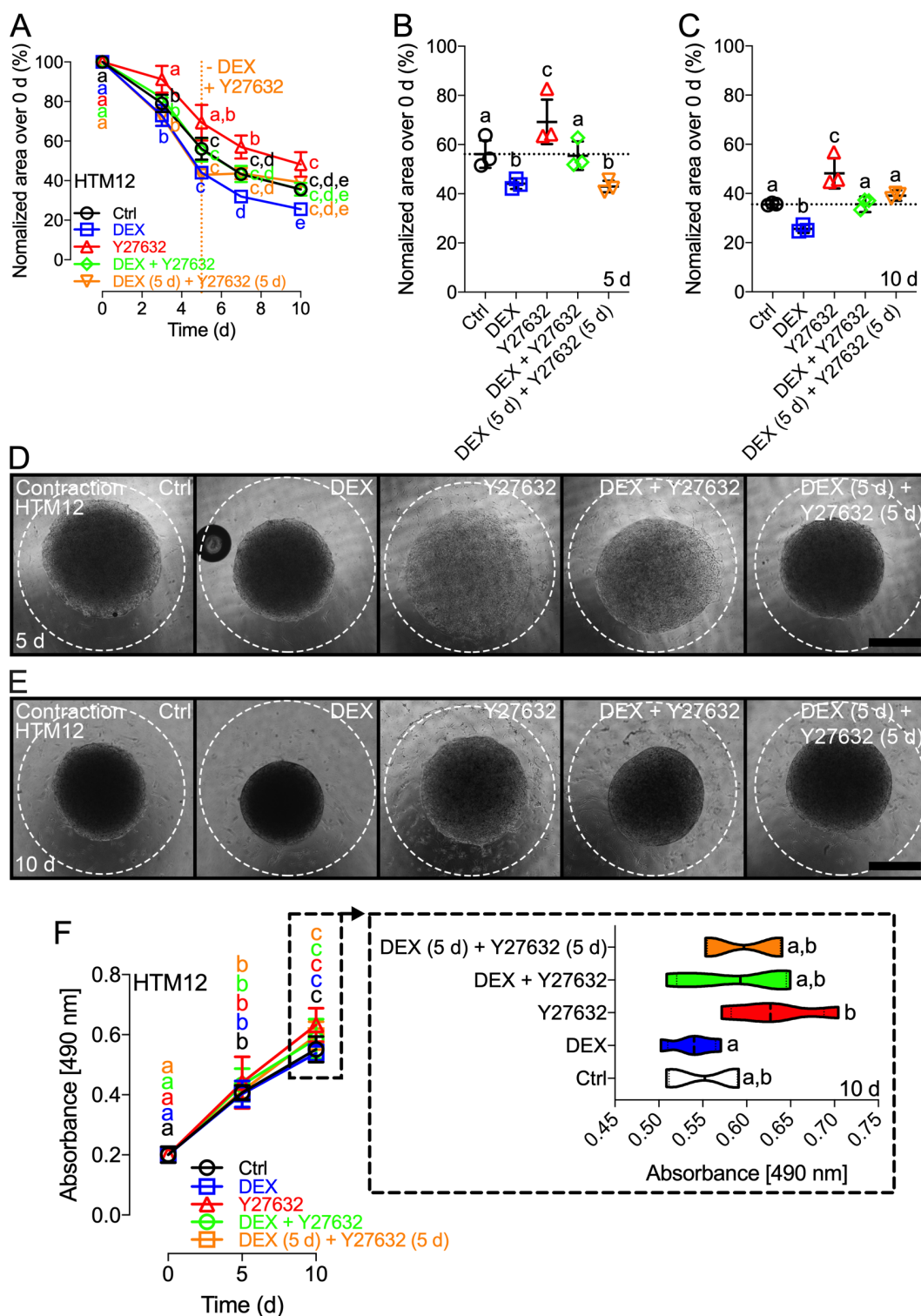
Fig. 7. HTM hydrogel contractility and cell proliferation with corticosteroid induction and ROCK inhibitor rescue. (**A**) Longitudinal quantification (i.e., construct size relative to 0 d) of HTM12 cell contractility in hydrogels subjected to control, 100 nM DEX, 10 μM Y27632, DEX

592 + Y27632, or DEX (5 d) + Y27632 (5 d) (N=3 per group; shared significance indicator letters
593 represent non-significant difference (p>0.05), distinct letters represent significant difference
594 (p<0.05)). Detailed comparisons between groups at (**B**) 5 d and (**C**) 10 d (dotted lines show
595 respective control values for reference). Representative brightfield images of HTM12 hydrogels
596 subjected to the different treatments at (**D**) 5 d and (**E**) 10 d; white dashed lines outline original
597 size of constructs at 0 d. Scale bars, 1 mm. (**F**) Longitudinal cell proliferation quantification of
598 HTM12 hydrogels subjected to the different treatments; dashed box shows detailed comparisons
599 between groups at 10 d (N=3 per group; shared significance indicator letters represent non-
600 significant difference (p>0.05), distinct letters represent significant difference (p<0.05)).

601

602 To validate the utility of the HTM hydrogel as glaucoma disease model, we next assessed an

603 alternative pair of pharmacological induction and rescue: transforming growth factor beta-2

604 (TGF-β2), implicated in the pathogenesis of POAG [63], and latrunculin-b (Lat-B), which prevents

605 polymerization of actin filaments [64]. Remarkably similar results to DEX/Y27632 were obtained.

606 We noted significant contraction over time in all groups (**Suppl. Fig. S6A**). TGF-β2-treated

607 HTM hydrogels showed significantly greater contraction vs. controls by 5 d, reaching ~45% of

608 their original size. Comparable values were observed in the sequential treatment samples (TGF-

609 β2 (5 d) + Lat-B (5 d); identical to TGF-β2 at this time point). Lat-B only slightly relaxed the

610 HTM hydrogels (~58% of their original size) vs. controls. Furthermore, no differences were

611 found between TGF-β2 + Lat-B co-treated samples and controls by 5 d, but constructs were

612 significantly less contracted compared to TGF-β2-treated HTM hydrogels; this suggests that Lat-

613 B can offset TGF-β2-induced pathologic contraction of HTM hydrogels when presented together

614 (**Suppl. Fig. S6A,B,D**). By 10 d, TGF-β2 treatment induced significantly more contraction (~25%

615 of their original size) vs. all other groups, while Lat-B treatment resulted in only slightly less

616 contraction (~44% of their original size) vs. controls. No differences were observed between

617 TGF-β2 + Lat-B co-treatment and controls. However, Lat-B rescued HTM hydrogel contraction

618 induced by TGF-β2; i.e., construct size with TGF-β2 (5 d) + Lat-B (5 d) sequential treatment was

619   similar to the control and TGF-β2 + Lat-B groups, but significantly increased compared to TGF-

620   β2-treated samples (**Suppl. Fig. S6A,C,E**).

621

622   ***Hydrogel actin rearrangement***

623   The actin cytoskeleton, the primary force-generating machinery in cells, plays fundamental roles

624   in various cellular process such as migration, morphogenesis, and cytokinesis [65]. Filamentous f-

625   actin fiber arrangement directly affects cell and tissue contraction. Therefore, we next

626   investigated f-actin and alpha smooth muscle actin (αSMA) abundance and organization in HTM

627   hydrogels subjected to the different treatments (**Fig. 8**). DEX-treated constructs showed

628   substantial reorganization of HTM cell microfilaments, with increased formation of f-actin/stress

629   fibers, minor actin tangles, and crosslinked actin network (CLAN)-like structures in the 3D

630   hydrogel environment vs. controls. By contrast, Y27632 treatment depolarized microfilaments

631   with notably decreased f-actin fibers compared to both control and DEX-treated groups. No

632   differences were observed for DEX + Y27632 co- or sequential treatment in comparison to

633   Y27632; again markedly decreased f-actin fibers were noted vs. control and DEX-treated groups

634   (**Fig. 8A**). Overall relatively similar trends were observed for αSMA. DEX-treated samples

635   showed substantially increased αSMA expression vs. all other groups, whereas Y27632 nearly

636   abolished the αSMA signal (high exposure chosen to illustrate this point). Again, no differences

637   were observed between DEX + Y27632 co- or sequential treatment, with comparable αSMA

638   expression to controls, but higher levels vs. Y27632-treated hydrogels (**Fig. 8B**).

639   Together, these data show that DEX increases f-actin fibers and α-SMA in HTM hydrogels,

640   which is potently rescued by Y27632. This is consistent with the reported reduction of

641   actomyosin contractile tone in HTM tissue following ROCK inhibition [22-25]. These changes in f-

642   actin and α-SMA could have a direct impact on HTM cell contractility and interactions with their

643   surrounding ECM, as well as HTM tissue stiffness and ultimately AH outflow resistance.

644

645
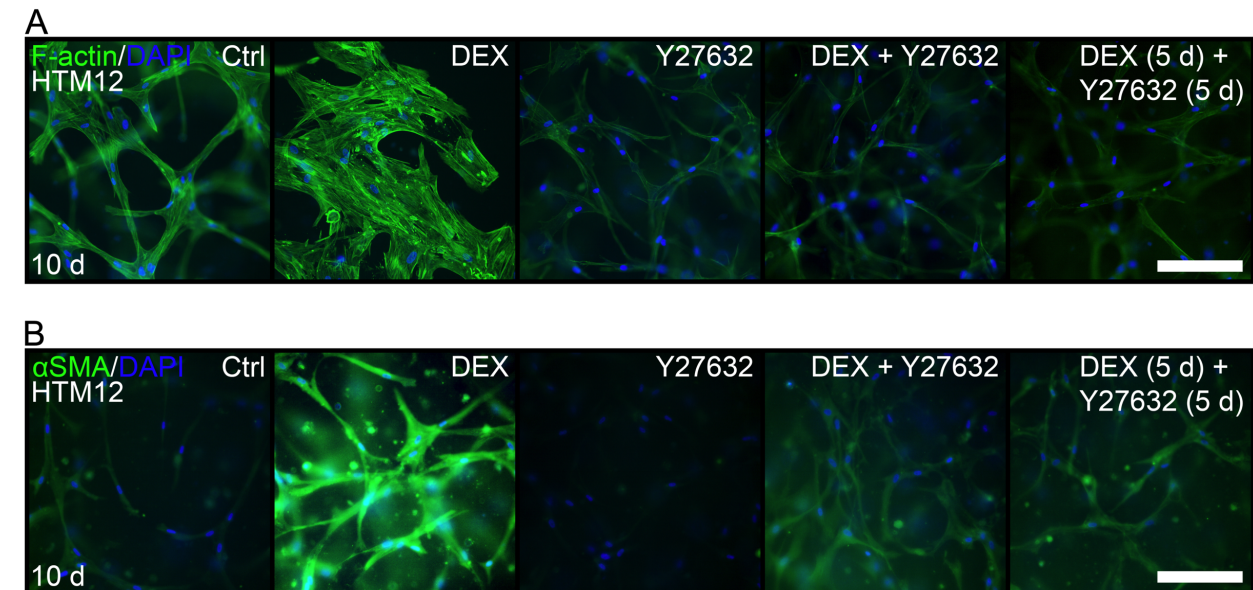
Fig. 8. F-actin and αSMA expression by HTM cells in hydrogels with corticosteroid
induction and ROCK inhibitor rescue. Representative fluorescence micrographs of (**A**) f-actin
and (**B**) αSMA in HTM12 hydrogels subjected to control, 100 nM DEX, 10 μM Y27632, DEX +
Y27632, or DEX (5 d) + Y27632 (5 d) at 10 d (f-actin and αSMA = green; DAPI = blue). Scale
bars, 250 μm.

651

Hydrogel morphology and ECM deposition

653   Continuous remodeling of baseline hydrogel ECM components (i.e., fibrillar collagen type I and

654   ELP, plus HA) and HTM cell-secreted ECM over culture time, and in response to the different

655   treatments is expected and desired. We next investigated overall morphology of HTM hydrogels

656   subjected to the different treatments using picrosirius red-stained sections (**Fig. 9A**). Consistent

657   with the contractility analyses, DEX-treated HTM hydrogels appeared condensed with decreased

658   inter-fibrillar spaces and reduced fiber thickness vs. controls. By contrast, Y27632 noticeably

659 increased the inter-fibrillar spaces compared to controls, while fiber thickness appeared largely

660 unaffected. DEX + Y27632 co- or sequential treatment were comparable to controls but overall

661 less dense vs. DEX-treated constructs. Of note, abundant hematoxylin-stained HTM cells were

662 visible across groups.

663 There is increased accumulation of ECM proteins in the HTM tissue of glaucomatous eyes [66].

664 Therefore, we next evaluated HTM cell-mediated fibronectin and collagen type IV deposition

665 within hydrogels in response to the different treatments (**Fig. 9B-D**). DEX-treated constructs

666 exhibited significantly more fibronectin deposition vs. controls (highest overall), whereas

667 Y27632 markedly reduced the fibronectin signal intensity. DEX + Y27632 co-treatment resulted

668 in significantly less fibronectin deposition (lowest overall) compared to the control and DEX

669 groups. Importantly, Y27632 rescued aberrant fibronectin deposition induced by DEX; i.e.,

670 significantly less signal intensity with DEX (5 d) + Y27632 (5 d) sequential treatment was noted

671 compared to DEX-treated samples (**Fig. 9B,D**). Similar trends (albeit not significant) were

672 observed for collagen IV, with overall lower expression compared to fibronectin (**Fig. 9C,D**).

673 Together, these data show that DEX induces HTM hydrogel condensation and remodeling, and

674 aberrant ECM deposition consistent with glaucomatous tissue dysfunction, which is largely

675 rescued with ROCK inhibition.

676
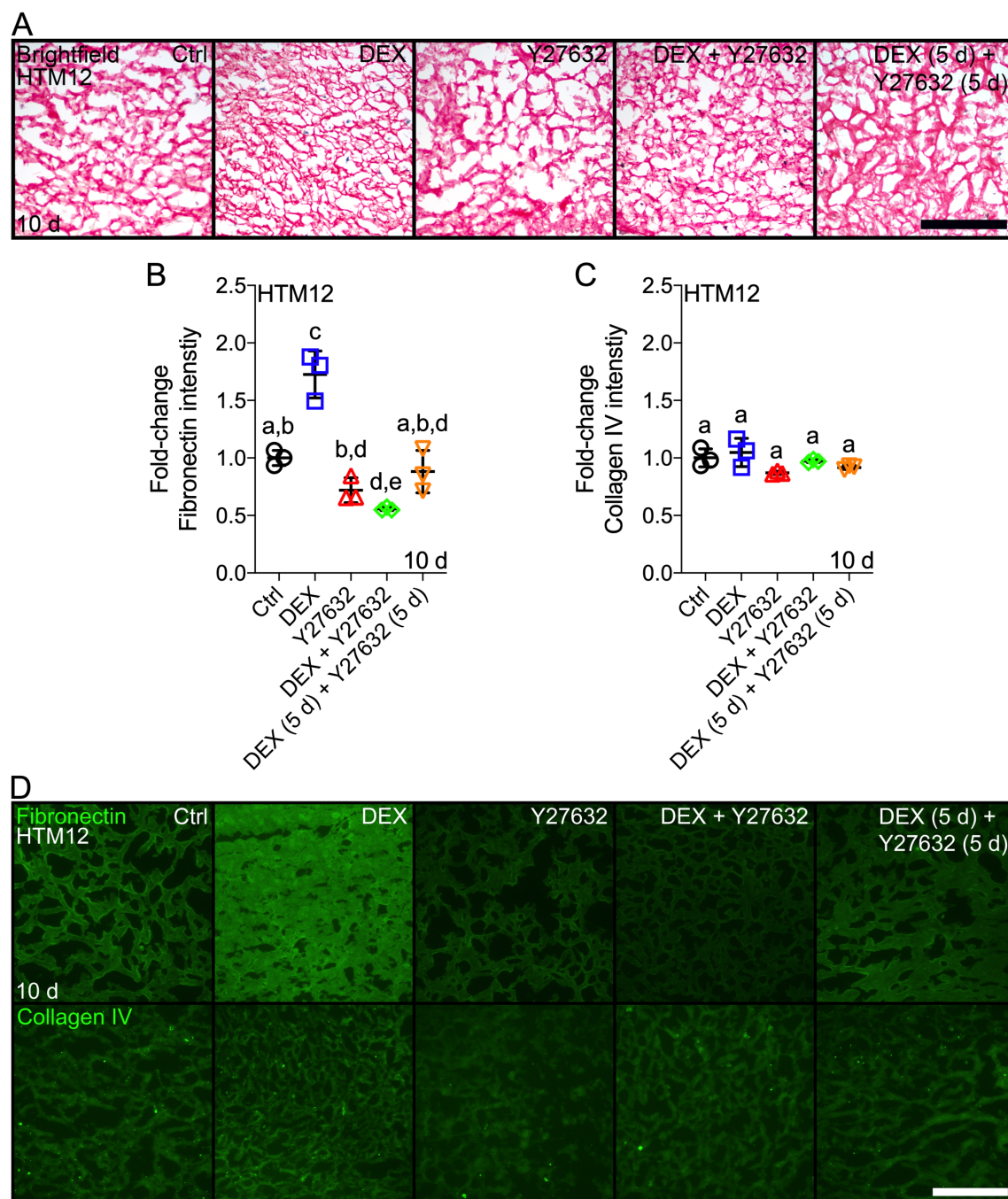
Fig. 9. HTM hydrogel morphology and ECM deposition with corticosteroid induction and ROCK inhibitor rescue. (**A**) Representative brightfield micrographs of picrosirius red/hematoxylin-stained sections from HTM12 hydrogels subjected to control, 100 nM DEX, 10 μM Y27632, DEX + Y27632, or DEX (5 d) + Y27632 (5 d) at 10 d (hydrogel/ECM = pink; HTM cells = blue). Scale bar, 250 μm (**B,C**) Quantification and (**D, E**) representative fluorescence micrographs of fibronectin and collagen IV (= green) in HTM12 hydrogels subjected to the different treatments at 10 d. Scale bar, 250 μm.

685

686   *Hydrogel stiffness*

687   Dysregulation of HTM cells and pathologic ECM remodeling jointly contribute to HTM

688   stiffening in POAG, which negatively affects IOP in a feed-forward loop [11-13]. To assess the

689   functional consequences of increased hydrogel contraction/condensation, driven by cytoskeletal

690   rearrangements and ECM remodeling/deposition, on tissue-level construct stiffness, we next

691   performed rheology analysis of HTM hydrogels subjected to the different treatments. We

692   determined fold-changes in storage modulus vs. 0 d for comparisons between groups (**Fig. 10A**).

693   DEX treatment significantly stiffened HTM hydrogels vs. control (~1.7-fold) consistent with

694   recent reports from normal and glaucomatous HTM tissues [13,67], while Y27632 had precisely

695   opposite effects and significantly softened HTM hydrogels vs. controls (~0.6-fold). No

696   differences were observed between DEX + Y27632 co-treatment and controls. Importantly,

697   Y27632 rescued pathologic HTM hydrogel stiffening induced by DEX and prevented further

698   stiffening; i.e., storage modulus with DEX (5 d) + Y27632 (5 d) sequential treatment was similar

699   to the control and DEX + Y27632 groups, but significantly lower compared to DEX-treated

700   samples (**Fig. 10A**). These findings were in agreement with HTM hydrogel contraction in this

701   large sample format (**Fig. 10B,C**), mirroring the trends observed with the 15x smaller samples

702   (**Fig. 6C**).

703   This suggests that DEX induces tissue-level HTM hydrogel contraction and stiffening consistent

704   with glaucomatous tissue behavior, and that ROCK inhibition effectively prevents or rescues

705   DEX-induced pathologic stiffening.

706
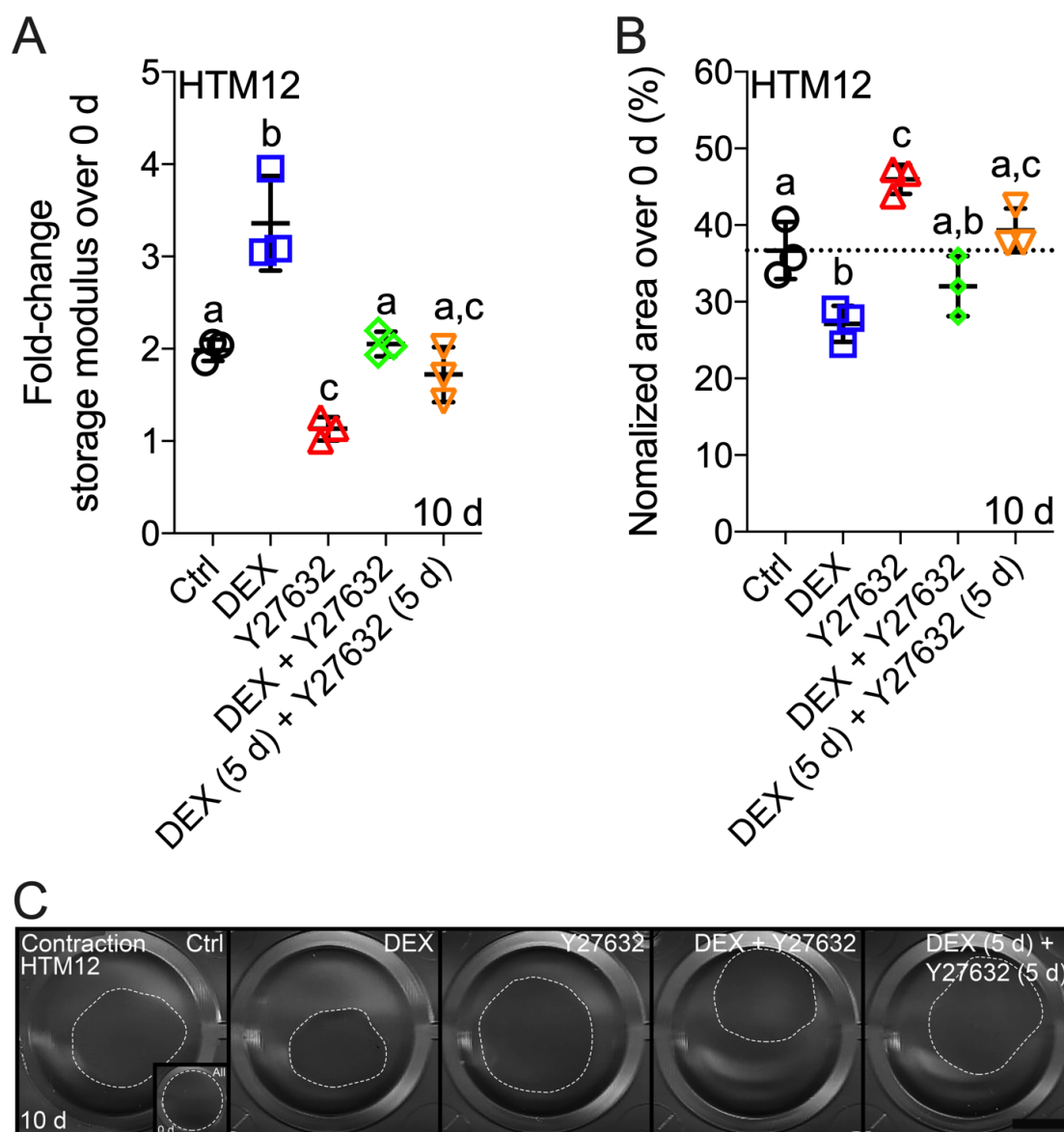
Fig. 10. HTM hydrogel stiffness with corticosteroid induction and ROCK inhibitor rescue.
(**A**) Fold-change in storage modulus (i.e., normalized to 0 d) of HTM12 hydrogels subjected to control, 100 nM DEX, 10 μM Y27632, DEX + Y27632, or DEX (5 d) + Y27632 (5 d) at 10 d (N=3 per group; shared significance indicator letters represent non-significant difference (p>0.05), distinct letters represent significant difference (p<0.05)). (**B**) Normalized contractility quantification (i.e., construct size relative to 0 d) of HTM12 hydrogels subjected to the different treatments at 10 d (N=3 per group; dotted line shows control values for reference; shared significance indicator letters represent non-significant difference (p>0.05), distinct letters represent significant difference (p<0.05)). (**C**) Representative scanned 24-well plate with HTM12 hydrogels subjected to the different treatments at 10 d (white dashed lines outline size of contracted constructs; inset, white dashed line outlines original size of all constructs [= entire well area] at 0 d). Scale bar, 5 mm.

Discussion

In vitro studies of HTM cell function are fundamentally limited by traditional cell culture systems. It is widely accepted that cells in 3D environments made of relevant ECM proteins show altered behavior compared to 2D, highlighting the need for more biologically-relevant HTM model systems [68,69]. Current bioengineered models [37,39-41,47-49,51,70] are useful tools for investigating aspects of HTM cell/tissue behavior under normal and simulated glaucomatous conditions, and complement proven *ex vivo* perfusion-cultured anterior segments and *in vivo* animal models. However, they cannot accurately mimic the complex native HTM cell-ECM interface, which makes them less than ideal to investigate the processes involved in the onset and progression of glaucomatous HTM stiffening typically observed with POAG. In this study, we used ECM proteins present in the native tissue to formulate a novel biomimetic 3D HTM hydrogel to provide a key advancement in bioengineered glaucoma disease modeling.

Our focus was to partially recapitulate the JCT region for both its critical role in regulating AH outflow resistance and IOP, and inextricable link to glaucomatous HTM tissue stiffening. HTM cells within the JCT are surrounded by fibrillar ECM components (i.e., collagen type I, elastin) to form a loose connective tissue rich in the glycosaminoglycan HA [3-7]. Proper maintenance of this HTM cell-ECM microenvironment is critical for homeostatic IOP regulation via normal ECM remodeling [4-7]. Protein-based hydrogels are widely used in tissue engineering applications as they provide a simplified version of the natural 3D tissue environment and allow for accurate *in vitro* modeling of cellular behaviors [42-46]. Photoactive functional groups (e.g., thiols, methacrylates) can be chemically conjugated to protein-based materials. These functionalized precursors can then be crosslinked by exposure to UV light in the presence of a biocompatible

744   photoinitiator, without or with cells, to form stable hydrogel networks with high water content [46].

745   Collagen type I and HA are frequently used for tissue engineering applications and

746   functionalized polymers are commercially available; however, incorporating elastin presents

747   certain challenges. In native tissues, elastic fibers are highly crosslinked and insoluble preventing

748   their direct processing for use in biomaterials [71]. Therefore, various forms of soluble elastin have

749   been engineered, including ELPs [72,73]. The key advantage of the unique ELP used herein is that it

750   is flanked by a short peptide sequence (KCTS) in which the two cysteines effectively act as

751   photoactive thiols [56]. A UV-crosslinked hydrogel containing ELP and HA was recently reported

752   [57]; however, no study to date has developed a biopolymer composite system with added collagen

753   type I, the most abundant fibrillar protein in the human body and main structural element of the

754   ECM [74].

755   We formulated a novel HTM hydrogel by mixing normal human donor-derived TM cells with

756   methacrylate-conjugated collagen type I, KCTS-flanked ELP, and thiol-conjugated HA followed

757   by photoinitiator-mediated short UV crosslinking. Informed by previous studies [75], we showed

758   excellent HTM cell viability (i.e., negligible cytotoxicity) in response to 5 s UV crosslinking at

759   the chosen conditions. This protein-based hydrogel created a supportive microenvironment to

760   facilitate prominent HTM cell spreading/proliferation throughout the adequately soft and porous

761   3D network. Of note, we estimated (acellular) hydrogel pore size at ~40 μm, which is larger than

762   that found in the JCT region but consistent with the central and outer lamellar regions [4,5,7].

763   Higher concentrations of biopolymer precursors could provide increased crosslinking density,

764   which may increase the hydrogel stiffness and consequently decrease pore size. Dynamic

765   interactions between HTM cells and their surrounding ECM resulted in hydrogel

766   condensation/contraction and remodeling, mimicking critical normal tissue behavior. As such,

767   our HTM cell-encapsulated hydrogel containing (by weight) ~68% collagen type I, ~26% ELP,

768   and ~5% HA is the first of its kind with distinct biomimetic advantages over other HTM model

769   systems [37,39-41,47-49,51,70].

770

771   Prolonged treatment with ocular corticosteroids such as DEX can lead to steroid-induced

772   elevation of IOP. This in turn can cause steroid-induced glaucoma, which has commonalities

773   with POAG; namely, increased HTM cell/tissue contraction and ECM deposition that can lead to

774   HTM stiffening and increased resistance to AH outflow [9,10,76,77]. Therefore, DEX is frequently

775   used to induce glaucomatous conditions in experimental studies [35]. Rho-associated kinases are

776   effectors of the small GTPase Rho, which play major roles in mediating the reorganization of the

777   actin cytoskeleton [78,79] with involvement in diseases such as pulmonary hypertension, nerve

778   injury, and POAG [80]. To that end, the recently approved ROCK inhibitor netarsudil [21] directly

779   targets the stiffened HTM to increase AH outflow via cell/tissue relaxation through reduction of

780   actomyosin contractile tone [22-26]. And while not without merit, current HTM model systems are

781   hampered by their inability to reliably and efficiently determine the relative contributions of

782   HTM cells and their ECM to the onset and progression of glaucomatous HTM stiffening. No *in*

783   *vitro* study to date has reported changes in tissue-level construct stiffness with DEX

784   challenge/Y27632 rescue. To assess the utility of our HTM hydrogel as glaucoma disease model,

785   we used proven corticosteroid induction of POAG-like conditions with DEX, and assessed the

786   therapeutic effects of ROCK inhibition with Y27632 on cell cytoskeletal organization and tissue-

787   level function dependent on HTM cell-ECM interactions.

788   We showed increased HTM hydrogel contraction with DEX treatment, which is opposite to what

789   a previous study found using simple collagen type I hydrogels encapsulated with bovine TM

790 cells [81], but consistent with data obtained from perfusion-cultured HTM tissues challenged with

791 DEX [76,77]. Actin abundance and organization are thought to modulate intracellular force

792 generation and cell contractility; our results showed that DEX induced elevated f-actin and

793 αSMA abundance and rearrangement, which is consistent with observations made using porous

794 scaffolds seeded with HTM cells [38]. This suggests that increased actin abundance could induce

795 cell contractile force generation to condense HTM cells within the 3D hydrogel network

796 resulting in overall increased construct contractility. HTM remodeling is critical for proper tissue

797 function, driven by the reciprocity between HTM cells and their ECM. By the same token,

798 pathologic ECM remodeling contributes to glaucomatous tissue dysfunction. We observed

799 increased microstructural ECM remodeling (i.e., condensed hydrogels with decreased inter-

800 fibrillar spaces and reduced fiber thickness) with DEX treatment. Furthermore, fibronectin - and

801 to a lesser extent collagen type IV - deposition induced by DEX was confirmed in our model,

802 which has been reported to contribute to elevated outflow resistance in the HTM with POAG [9].

803 These findings are in agreement with glaucomatous pathology and have all been linked to

804 progressive HTM tissue stiffening. Importantly, consistent with the reported reduction of

805 actomyosin contraction in HTM tissue following ROCK inhibition [22-25], we showed that Y27632

806 co-treatment (simulating a prophylactic approach) and sequential treatment (simulating a

807 therapeutic approach) potently rescued the DEX-induced pathologic changes in HTM hydrogel

808 contractility, condensation, and ECM deposition/remodeling. Using an alternative pair of

809 pharmacological induction and rescue of glaucomatous conditions - TGF-β2 (a potent cytokine

810 implicated in POAG pathology [63]) and Lat-B (an actin filament depolymerizing agent [64]), we

811 were able to validate the utility of our HTM hydrogel as glaucoma disease model.

812

813   Patients with POAG, the most common subtype of glaucoma, typically suffer from elevated IOP

814   and experience increased HTM stiffness, which in turn can negatively affect IOP and HTM cell

815   function in a feed-forward loop [9-13]. It is perhaps because of these observations that more studies

816   in recent years have focused on the biomechanical properties of tissues within the conventional

817   outflow pathway, and their dynamic changes in disease. HTM tissue stiffness has been

818   determined directly and indirectly in several studies. In an early report, HTM stiffness was

819   shown to be ~20-fold higher in glaucomatous vs. normal eyes by atomic force microscopy

820   (AFM) [11]. Several limitations to this study, however, may have resulted in overestimated

821   differences in tissue elasticity. In a recent elegant study using a novel indirect approach (with

822   AFM correlation), HTM stiffness was determined to be ~1.4-fold greater in glaucomatous HTM

823   tissues vs. normal controls [13,67]. The discrepancies in both absolute and relative stiffness values

824   (i.e., normal vs. glaucomatous) between the two studies most likely stem from methodological

825   differences. We here showed an ~1.7-fold increase in HTM hydrogel stiffness with DEX

826   treatment vs. controls as measured by rheology (oscillatory shear-strain sweep test), a common

827   technique for characterizing biomechanical properties of viscoelastic hydrogels. Y27632

828   treatment had precisely opposite effects, and was shown to prevent or rescue the DEX-induced

829   pathologic changes, resulting in HTM hydrogel softening. This was in agreement with the HTM

830   hydrogel contraction, cytoskeletal rearrangement, and ECM remodeling/deposition data

831   suggesting potent therapeutic potential of Y27632 in support of clinical netarsudil use. While we

832   can only speculate on the corresponding hydrogel stiffness values by AFM, previous studies

833   have suggested good overall correlation between the two methods [82,83], with trends frequently

834   being preserved.

835

836   Elevated AH outflow resistance and IOP are directly related to retinal ganglion cell damage in

837   POAG. We acknowledge that a limitation to our system is the lack of flow. Ongoing work to

838   integrate the HTM hydrogel, with addition of a Schlemm's canal endothelial cell layer, on a

839   microfluidics platform for measurements of flow resistance under dynamic conditions is

840   expected to further expand the utility of our hydrogel-based glaucoma disease model. ECM

841   stiffness is considered a universal mechanical cue that can both precede and propel disease by

842   altering the behavior of associated cells according to the changing ECM elasticity. In diseases

843   such as idiopathic lung fibrosis and multiple myeloma, there are clinical trials underway that

844   directly target ECM remodeling to prevent pathologic tissue stiffening [30]. If matrix stiffness is a

845   driving factor that causes the ECM to further stiffen under pathological conditions, then what are

846   the initial mechanisms contributing to pre-pathological increases in matrix rigidity? A key

847   advantage of our HTM hydrogel is the ability to tune construct stiffness. Ongoing work explores

848   the potential of targeting relevant mechanotransduction pathways for POAG therapy.

849

850   In sum, we have developed a novel *in vitro* biomimetic HTM hydrogel model that allows for

851   detailed investigation of the 3D HTM cell-ECM interface under normal and simulated POAG

852   conditions upon *in situ* corticosteroid induction. Importantly, unlike other model systems, the

853   HTM biopolymer hydrogel enables correlative analyses of HTM cell cytoskeletal organization

854   with tissue-level functional changes - glaucomatous pathologic contraction and stiffening -

855   contingent on HTM cell-ECM interactions. The bidirectional responsiveness of the HTM

856   hydrogel model system to pharmaceutical challenge and rescue suggests promising potential to

857   serve as a screening platform for new POAG treatments with focus on HTM cell/tissue

858   biomechanics.

859

References

1. Gould DB, John SWM. Anterior segment dysgenesis and the developmental glaucomas are complex traits. *Human Molecular Genetics* 2002;11:1185-1193.

2. Brubaker RF. Flow of aqueous humor in humans [The Friedenwald Lecture]. *Invest Ophthalmol Vis Sci* 1991;32:3145-3166.

3. Keller KE, Acott TS. The Juxtacanalicular Region of Ocular Trabecular Meshwork: A Tissue with a Unique Extracellular Matrix and Specialized Function. *J Ocul Biol* 2013;1:3.

4. Acott TS, Kelley MJ. Extracellular matrix in the trabecular meshwork. *Exp Eye Res* 2008;86:543-561.

5. Tamm ER. The trabecular meshwork outflow pathways: structural and functional aspects. *Exp Eye Res* 2009;88:648-655.

6. Hann CR, Fautsch MP. The elastin fiber system between and adjacent to collector channels in the human juxtacanalicular tissue. *Invest Ophthalmol Vis Sci* 2011;52:45-50.

7. Abu-Hassan DW, Acott TS, Kelley MJ. The Trabecular Meshwork: A Basic Review of Form and Function. *J Ocul Biol* 2014;2:9.

8. Kelley MJ, Rose AY, Keller KE, Hessle H, Samples JR, Acott TS. Stem cells in the trabecular meshwork: present and future promises. *Exp Eye Res* 2009;88:747-751.

9. Faralli JA, Filla MS, Peters DM. Role of Fibronectin in Primary Open Angle Glaucoma. *Cells* 2019;8.

10. Ramos RF, Sumida GM, Stamer WD. Cyclic Mechanical Stress and Trabecular Meshwork Cell Contractility. *Investigative Ophthalmology & Visual Science* 2009;50:3826-3832.

902   11.   Last JA, Pan T, Ding Y, et al. Elastic modulus determination of normal and glaucomatous

903   human trabecular meshwork. *Invest Ophthalmol Vis Sci* 2011;52:2147-2152.

904   12.   Stamer WD, Acott TS. Current understanding of conventional outflow dysfunction in

905   glaucoma. *Curr Opin Ophthalmol* 2012;23:135-143.

906   13.   Wang K, Johnstone MA, Xin C, et al. Estimating Human Trabecular Meshwork Stiffness

907   by Numerical Modeling and Advanced OCT Imaging. *Invest Ophthalmol Vis Sci* 2017;58:4809-

908   4817.

909   14.   Quigley HA. Open-angle glaucoma. *N Engl J Med* 1993;328:1097-1106.

910   15.   Quigley HA, Broman AT. The number of people with glaucoma worldwide in 2010 and

911   2020. *Br J Ophthalmol* 2006;90:262-267.

912   16.   Kwon YH, Fingert JH, Kuehn MH, Alward WL. Primary open-angle glaucoma. *N Engl J*

913   *Med* 2009;360:1113-1124.

914   17.   Tham YC, Li X, Wong TY, Quigley HA, Aung T, Cheng CY. Global prevalence of

915   glaucoma and projections of glaucoma burden through 2040: a systematic review and meta-

916   analysis. *Ophthalmology* 2014;121:2081-2090.

917   18.   Tamm ER, Braunger BM, Fuchshofer R. Intraocular Pressure and the Mechanisms

918   Involved in Resistance of the Aqueous Humor Flow in the Trabecular Meshwork Outflow

919   Pathways. *Prog Mol Biol Transl Sci* 2015;134:301-314.

920   19.   Beidoe G, Mousa SA. Current primary open-angle glaucoma treatments and future

921   directions. *Clin Ophthalmol* 2012;6:1699-1707.

922   20.   Lin CW, Sherman B, Moore LA, et al. Discovery and Preclinical Development of

923   Netarsudil, a Novel Ocular Hypotensive Agent for the Treatment of Glaucoma. *J Ocul*

924   *Pharmacol Ther* 2018;34:40-51.

925   21.   Serle JB, Katz LJ, McLaurin E, et al. Two Phase 3 Clinical Trials Comparing the Safety

926   and Efficacy of Netarsudil to Timolol in Patients With Elevated Intraocular Pressure: Rho

927   Kinase Elevated IOP Treatment Trial 1 and 2 (ROCKET-1 and ROCKET-2). *Am J Ophthalmol*

928   2018;186:116-127.

929   22.   Rao PV, Deng PF, Kumar J, Epstein DL. Modulation of aqueous humor outflow facility

930   by the Rho kinase-specific inhibitor Y-27632. *Invest Ophthalmol Vis Sci* 2001;42:1029-1037.

931   23.   Wang SK, Chang RT. An emerging treatment option for glaucoma: Rho kinase

932   inhibitors. *Clin Ophthalmol* 2014;8:883-890.

933   24.   Tanna AP, Johnson M. Rho Kinase Inhibitors as a Novel Treatment for Glaucoma and

934   Ocular Hypertension. *Ophthalmology* 2018;125:1741-1756.

935   25.   Rao PV, Pattabiraman PP, Kopczynski C. Role of the Rho GTPase/Rho kinase signaling

936   pathway in pathogenesis and treatment of glaucoma: Bench to bedside research. *Exp Eye Res*

937   2017;158:23-32.

938   26.   Zhang K, Zhang L, Weinreb RN. Ophthalmic drug discovery: novel targets and

939   mechanisms for retinal diseases and glaucoma. *Nat Rev Drug Discov* 2012;11:541-559.

940   27.   Dasso L, Al-Khaled T, Sonty S, Aref AA. Profile of netarsudil ophthalmic solution and

941   its potential in the treatment of open-angle glaucoma: evidence to date. *Clin Ophthalmol*

942   2018;12:1939-1944.

943   28.   Tanna AP, Esfandiari H, Teramoto K. Reversible Corneal Endothelial Abnormalities

944   with Netarsudil. *J Glaucoma* 2020.

945   29.   Wisely CE, Liu KC, Gupta D, Carlson AN, Asrani SG, Kim T. Reticular Bullous

946   Epithelial Edema in Corneas Treated with Netarsudil: A Case Series. *Am J Ophthalmol* 2020.

947   30.   Lampi MC, Reinhart-King CA. Targeting extracellular matrix stiffness to attenuate

948   disease: From molecular mechanisms to clinical trials. *Sci Transl Med* 2018;10:eaao0475.

949   31.   Paylakhi SH, Yazdani S, April C, et al. Non-housekeeping genes expressed in human

950   trabecular meshwork cell cultures. *Molecular vision* 2012;18:241-254.

951   32.   Stamer WD, Williams AM, Pflugfelder S, Coupland SE. Accessibility to and Quality of

952   Human Eye Tissue for Research: A Cross-Sectional Survey of ARVO Members. *Invest*

953   *Ophthalmol Vis Sci* 2018;59:4783-4792.

954   33.   Fan BJ, Wang DY, Tham CCY, Lam DSC, Pang CP. Gene Expression Profiles of Human

955   Trabecular Meshwork Cells Induced by Triamcinolone and Dexamethasone. *Investigative*

956   *Ophthalmology & Visual Science* 2008;49:1886-1897.

957   34.   Gerometta R, Podos SM, Candia OA, et al. Steroid-induced ocular hypertension in

958   normal cattle. *Arch Ophthalmol* 2004;122:1492-1497.

959   35.   Rybkin I, Gerometta R, Fridman G, Candia O, Danias J. Model systems for the study of

960   steroid-induced IOP elevation. *Exp Eye Res* 2017;158:51-58.

961   36.   Langer R, Vacanti JP. Tissue engineering. *Science* 1993;260:920-926.

962   37.   Torrejon KY, Papke EL, Halman JR, et al. TGFβ2-induced outflow alterations in a

963   bioengineered trabecular meshwork are offset by a rho-associated kinase inhibitor. *Sci Rep*

964   2016;6:38319.

965   38.   Torrejon KY, Papke EL, Halman JR, et al. Bioengineered glaucomatous 3D human

966   trabecular meshwork as an in vitro disease model. *Biotechnol Bioeng* 2016;113:1357-1368.

967   39.   Torrejon KY, Pu D, Bergkvist M, Danias J, Sharfstein ST, Xie Y. Recreating a human

968   trabecular meshwork outflow system on microfabricated porous structures. *Biotechnol Bioeng*

969   2013;110:3205-3218.

970   40.   Osmond M, Bernier SM, Pantcheva MB, Krebs MD. Collagen and collagen-chondroitin

971   sulfate scaffolds with uniaxially aligned pores for the biomimetic, three dimensional culture of

972   trabecular meshwork cells. *Biotechnol Bioeng* 2017;114:915-923.

973   41.   Osmond MJ, Krebs MD, Pantcheva MB. Human Trabecular Meshwork Cell Behavior is

974   Influenced by Collagen Scaffold Pore Architecture and Glycosaminoglycan Composition.

975   *Biotechnol Bioeng* 2020.

976   42.   Lee KY, Mooney DJ. Hydrogels for tissue engineering. *Chem Rev* 2001;101:1869-1879.

977   43.   Khademhosseini A, Langer R. Microengineered hydrogels for tissue engineering.

978   *Biomaterials* 2007;28:5087-5092.

979   44.   Seliktar D. Designing cell-compatible hydrogels for biomedical applications. *Science*

980   2012;336:1124-1128.

981   45.   Green JJ, Elisseeff JH. Mimicking biological functionality with polymers for biomedical

982   applications. *Nature* 2016;540:386-394.

983   46.   Zhang YS, Khademhosseini A. Advances in engineering hydrogels. *Science*

984   2017;356:eaaf3627.

985   47.   Bouchemi M, Roubeix C, Kessal K, et al. Effect of benzalkonium chloride on trabecular

986   meshwork cells in a new in vitro 3D trabecular meshwork model for glaucoma. *Toxicol In Vitro*

987   2017;41:21-29.

988   48.   Vernazza S, Tirendi S, Scarfi S, et al. 2D- and 3D-cultures of human trabecular

989   meshwork cells: A preliminary assessment of an in vitro model for glaucoma study. *PLoS One*

990   2019;14:e0221942.

991   49.   Saccà SC, Tirendi S, Scarfi S, et al. An advanced in vitro model to assess glaucoma

992   onset. *ALTEX - Alternatives to animal experimentation* 2020;37(2):265-274.

993   50.   Caliari SR, Burdick JA. A practical guide to hydrogels for cell culture. *Nat Methods*

994   2016;13:405-414.

995   51.   Waduthanthri KD, He Y, Montemagno C, Cetinel S. An injectable peptide hydrogel for

996   reconstruction of the human trabecular meshwork. *Acta Biomaterialia* 2019;100:244-254.

997   52.   Koga T, Koga T, Awai M, Tsutsui J, Yue BY, Tanihara H. Rho-associated protein kinase

998   inhibitor, Y-27632, induces alterations in adhesion, contraction and motility in cultured human

999   trabecular meshwork cells. *Exp Eye Res* 2006;82:362-370.

1000   53.   Stamer WD, Seftor RE, Williams SK, Samaha HA, Snyder RW. Isolation and culture of

1001   human trabecular meshwork cells by extracellular matrix digestion. *Curr Eye Res* 1995;14:611-

1002   617.

1003   54.   Keller KE, Bhattacharya SK, Borras T, et al. Consensus recommendations for trabecular

1004   meshwork cell isolation, characterization and culture. *Exp Eye Res* 2018;171:164-173.

1005   55.   Schmittgen TD, Livak KJ. Analyzing real-time PCR data by the comparative C(T)

1006   method. *Nat Protoc* 2008;3:1101-1108.

1007   56.   Zhang YN, Avery RK, Vallmajo-Martin Q, et al. A Highly Elastic and Rapidly

1008   Crosslinkable Elastin-Like Polypeptide-Based Hydrogel for Biomedical Applications. *Adv Funct*

1009   *Mater* 2015;25:4814-4826.

1010   57.   Shirzaei Sani E, Portillo-Lara R, Spencer A, et al. Engineering Adhesive and

1011   Antimicrobial Hyaluronic Acid/Elastin-like Polypeptide Hybrid Hydrogels for Tissue

1012   Engineering Applications. *ACS Biomaterials Science & Engineering* 2018;4:2528-2540.

1013   58.   Siegner A, May CA, Welge-Lüssen UW, Bloemendal H, Lütjen-Drecoll E. alpha B-

1014   crystallin in the primate ciliary muscle and trabecular meshwork. *Eur J Cell Biol* 1996;71:165-

1015   169.

1016 59.   Tektas O-Y, Lütjen-Drecoll E. Structural changes of the trabecular meshwork in different

1017   kinds of glaucoma. *Experimental Eye Research* 2009;88:769-775.

1018 60.   van Oosten ASG, Chen X, Chin L, et al. Emergence of tissue-like mechanics from

1019   fibrous networks confined by close-packed cells. *Nature* 2019;573:96-101.

1020 61.   Dismuke WM, Liang J, Overby DR, Stamer WD. Concentration-related effects of nitric

1021   oxide and endothelin-1 on human trabecular meshwork cell contractility. *Exp Eye Res*

1022   2014;120:28-35.

1023 62.   Overby DR, Clark AF. Animal models of glucocorticoid-induced glaucoma.

1024   *Experimental eye research* 2015;141:15-22.

1025 63.   Lutjen-Drecoll E. Morphological changes in glaucomatous eyes and the role of TGFbeta2

1026   for the pathogenesis of the disease. *Exp Eye Res* 2005;81:1-4.

1027 64.   Rasmussen CA, Kaufman PL, Ritch R, Haque R, Brazzell RK, Vittitow JL. Latrunculin

1028   B Reduces Intraocular Pressure in Human Ocular Hypertension and Primary Open-Angle

1029   Glaucoma. *Transl Vis Sci Technol* 2014;3:1.

1030 65.   Svitkina T. The Actin Cytoskeleton and Actin-Based Motility. *Cold Spring Harb*

1031   *Perspect Biol* 2018;10:a018267.

1032 66.   Stamer WD, Clark AF. The many faces of the trabecular meshwork cell. *Exp Eye Res*

1033   2017;158:112-123.

1034 67.   Wang K, Read AT, Sulchek T, Ethier CR. Trabecular meshwork stiffness in glaucoma.

1035   *Exp Eye Res* 2017;158:3-12.

1036 68.   Bhadriraju K, Chen CS. Engineering cellular microenvironments to improve cell-based

1037   drug testing. *Drug Discov Today* 2002;7:612-620.

1038   69.   Edmondson R, Broglie JJ, Adcock AF, Yang L. Three-dimensional cell culture systems

1039   and their applications in drug discovery and cell-based biosensors. *Assay Drug Dev Technol*

1040   2014;12:207-218.

1041   70.   Dautriche CN, Szymanski D, Kerr M, et al. A biomimetic Schlemm's canal inner wall: A

1042   model to study outflow physiology, glaucoma pathology and high-throughput drug screening.

1043   *Biomaterials* 2015;65:86-92.

1044   71.   Mithieux SM, Weiss AS. Elastin. *Adv Protein Chem* 2005;70:437-461.

1045   72.   Daamen WF, Veerkamp JH, van Hest JC, van Kuppevelt TH. Elastin as a biomaterial for

1046   tissue engineering. *Biomaterials* 2007;28:4378-4398.

1047   73.   Nettles DL, Chilkoti A, Setton LA. Applications of elastin-like polypeptides in tissue

1048   engineering. *Adv Drug Deliv Rev* 2010;62:1479-1485.

1049   74.   Frantz C, Stewart KM, Weaver VM. The extracellular matrix at a glance. *J Cell Sci*

1050   2010;123:4195-4200.

1051   75.   Mazzocchi A, Devarasetty M, Herberg S, et al. Pleural Effusion Aspirate for Use in 3D

1052   Lung Cancer Modeling and Chemotherapy Screening. *ACS Biomaterials Science & Engineering*

1053   2019;5:1937-1943.

1054   76.   Johnson DH, Bradley JM, Acott TS. The effect of dexamethasone on

1055   glycosaminoglycans of human trabecular meshwork in perfusion organ culture. *Investigative*

1056   *Ophthalmology & Visual Science* 1990;31:2568-2571.

1057   77.   Johnson M. 'What controls aqueous humour outflow resistance?'. *Exp Eye Res*

1058   2006;82:545-557.

1059   78.   Riento K, Ridley AJ. ROCKs: multifunctional kinases in cell behaviour. *Nature Reviews*

1060   *Molecular Cell Biology* 2003;4:446-456.

1061   79.   Leung T, Manser E, Tan L, Lim L. A novel serine/threonine kinase binding the Ras-

1062   related RhoA GTPase which translocates the kinase to peripheral membranes. *J Biol Chem*

1063   1995;270:29051-29054.

1064   80.   Amano M, Nakayama M, Kaibuchi K. Rho-kinase/ROCK: A key regulator of the

1065   cytoskeleton and cell polarity. *Cytoskeleton (Hoboken)* 2010;67:545-554.

1066   81.   Duffy L, O'Reilly S. Functional Implications of Cross-Linked Actin Networks in

1067   Trabecular Meshwork Cells. *Cellular Physiology and Biochemistry* 2018;45:783-794.

1068   82.   Cruz-Acuna R, Quiros M, Farkas AE, et al. Synthetic hydrogels for human intestinal

1069   organoid generation and colonic wound repair. *Nat Cell Biol* 2017;19:1326-1335.

1070   83.   Phelps EA, Enemchukwu NO, Fiore VF, et al. Maleimide cross-linked bioactive PEG

1071   hydrogel exhibits improved reaction kinetics and cross-linking for cell encapsulation and in situ

1072   delivery. *Adv Mater* 2012;24:64-70, 62.

1073